Helmut Krasa, BSc

Deposition and characterization of Al(Ti)N thin films deposited by plasma enhanced atomic layer deposition

MASTER'S THESIS

to achieve the university degree of

Dipl.-Ing.

Master's degree programme: Technical Physics

submitted to

Graz University of Technology

Coclite, Anna Maria, Assoc. Prof. Dr.

Institut für Festkörperphysik

Graz, September 2020

AFFIDAVIT

I declare that I have authored this thesis independently, that I have not used other than the declared sources/resources, and that I have explicitly indicated all material which has been quoted either literally or by content from the sources used. The text document uploaded to TUGRAZonline is identical to the present master's thesis.

Date, Signature

Abstract

Titanium aluminum nitride is a wurtzite structure semiconductor with interesting mechanical and electrical properties. While titanium nitride has been widely studied and is used as a diffusion barrier for integrated circuit devices in the semiconductor industry, aluminum titanium nitride shows improved corrosion resistance and antioxidation properties. It therefore has the potential to be used in a wider selection of processing techniques allowing for greater flexibility.

Atomic layer deposition (ALD) is a form of chemical vapor deposition showing self-limiting growth properties and thickness control in the sub-nanometer regime. The deposition process in use is highly conformal and is an evolution of the conventional thermal ALD process. Plasma enhanced atomic layer deposition (PEALD) provides more freedom in the material selection and process conditions due to its increased reactivity.

This work aims at illustrating the optimization of the deposition process and analyzing the composition and structure of the produced thin films. Aluminum nitride thin films were deposited by PEALD using a Al-precursor and N_2 plasma as co-reactant. The doping with titanium was attempted by alternating a Ti-precursor to the Al-precursor in some of the PEALD cycles. X-ray reflectivity, x-ray diffraction, spectroscopic ellipsometry and Fourier transform infrared spectroscopy measurements were performed to characterize the thin films.

Kurzfassung

Aluminiumtitannitrid ist ein Halbleiter mit interessanten mechanischen und elektrischen Eigenschaften, welcher in der Wurtzite Struktur vorliegt. Während die Forschung von Titannitrid bereits fortgeschritten ist und als Diffusionsbarriere in integrierten Schaltkreisen bereits Anwendung findet, hat Aluminiumtitannitrid erhöhte Korrosions- und Oxidationsbeständigkeit. Dies ermöglicht den Einsatz weiterer Produktionsmechanismen und erhöht die Flexibilität in der Herstellung.

Atomlagenbeschichtung ist eine Form der chemischen Gasphasenabscheidung und zeichnet sich durch selbstlimitierendes Wachstum und Kontrolle der Filmdicke im Subnanometerbereich aus. Der verwendete Beschichtungsprozess ist höchst konform und eine Weiterentwicklung der klassischen, thermischen Atomlagenbeschichtung. Plasmaunterstütze Atomlagenbeschichtung weist eine erhöhte Reaktivität auf und ermöglicht eine breitere Auswahl der Materrialen und Prozessparameter.

Ziel dieser Arbeit ist es, den Beschichtungsprozess zu optimieren und die Struktur des erzeugten Dünnfilms zu analysieren. Aluminiumnitratfilme wurden mit Stickstoffplasma als Co-Reaktanten und Aluminium-Precursor deponiert. Das Doping von Titannitrat wurde mit einer abwechselnden Folge von Titan-Precursor und Aluminium-Precursor versucht. Röntgenreflektivität, Röntgendiffraktometrie, spektroskopische Ellipsometrie sowie Fourier-Transform-Infrarotspektrometrie wurde verwendet, um die Dünnfilme zu charakterisieren.

Acknowledgement

First of all, I want to thank my supervisor Assoc. Prof. Anna Maria Coclite for making this thesis possible. I was extremely lucky to have her as my supervisor as she guided me through the work, motivated me and was always there for advice when necessary.

Special thanks go to Stefan Pachmajer, with whom I reconstructed and worked on the experimental setup. He taught me a lot about laboratory work, it was a pleasure to work with you.

I am thankful for Roland Resel and his research group for constructive feedback and discussion we had during our group meetings.

I also would like to thank Harald Kerschbaumer, who was always there for me for technical support and eager to help if problems arised.

I also want to thank my colleagues of the CVD-ALD research group including Kathrin Unger, Martin Seiler, Marianne Kräuter, Richard Berger, Taher Abu Ali, Clarissa Holzer, Fabian Muralter, and Paul Kindlhofer for their input and help during the thesis and the great working athmosphere.

Furthermore, I am grateful of my study colleagues that quickly became friends (we called ourself "The Band") for their support during the first tough years of study. Just to name a few of them, I would like to thank Andreas, Markus, Gerald, Philipp, Tim and especially Michael for all their help. If it were not for you guys, I wouldn't be where I am now.

I also want to thank my friends Julia and Lukas for their input on my thesis.

Most of all, I want to thank my parents for their love, emotional and financial support during all my student life.

Contents

List of Figures

1 Fundamentals

In the following chapter the fundamentals of atomic layer deposition are described to give a basic understanding of the process within the scope of this thesis. A closer examination can be found either in *Atomic Layer Deposition of Nanostructured Materials* by Pinna and Knez [1] or in chapter 27 of *Handbook of Crystal Growth: Thin Films and Epitaxy: Second Edition* by Knoops et al. [2]. A review letter written by Profijt et al. [3] also gives a great insight into the topic, focusing mainly on the aspects which were introduced with the use of plasma during ALD process.

1.1 Principles of atomic layer deposition

Atomic **l**ayer **d**eposition (**ALD**) is a cyclic processing technique that allows the growth of ultra-thin films in the sub- nanometer scale. This method allows for thickness control in the nm-regime. Its development started in the 1960s in the Soviet Union and Finland under the name of atomic layer epitaxy. With further miniaturization in the semiconductor industry, a deposition technique which allows for thickness control on the atomic scale and conformal deposition of non-planar surfaces was necessary. This development was the major force behind the progress in ALD. Intel, the world's largest manufacturer of computer processors, uses ALD as a step to produce their so-called "tri-gate" transistors. It was introduced in their 22 nm FinFET process and later scaled down to 14 nm. The process is also used in DRAM capacitors and therefore the ALD process finds its way in almost every PC or laptop we use nowadays.[4]

In a conventional **c**hemical **v**apor **d**eposition (**CVD**) process, all molecules react with each other at the deposition temperature. In ALD, the exposed

molecules react only with the surface, but not with themselves. In this process at least two (possibly more - in case of this thesis three) different precursors are introduced in the reaction chamber in cycles to have them only react with the surface. Each precursor dose is separated by a purge dose in the vapor chamber so that remaining molecules in the reaction chamber are removed in order to avoid reactions in the vapor phase. This leads to a surface controlled, self-limiting process, in which not the exposure time, but the number of cycles determines the growth of the thin film. The growth rate is usually given in **g**rowth **p**er **c**ycle (GPC),is ideally is as high as one monolayer, but usually lies in the range of 0,05-0,1 nm/cycle due to steric effects . [3]

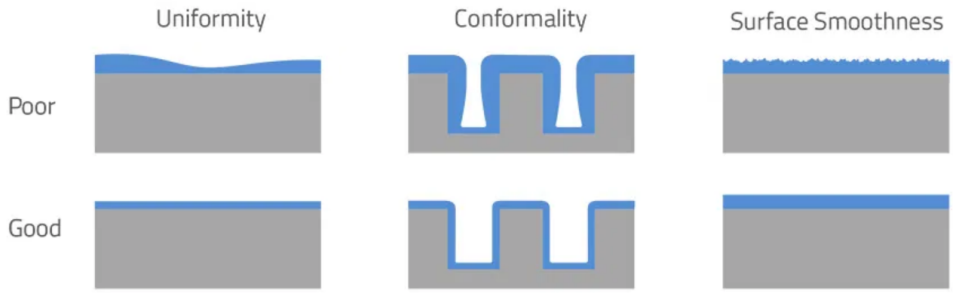

Figure 1.1: Idealized characteristics of an ALD thin film. Reprinted from [5]

The cyclic process is very time consuming (in practice each process step takes several seconds), which puts an upper limit to the maximum thickness of the film. The upside is a very precise thickness control and homogenity since the process is self-limiting. The lower images of figure 1.1 illustrates the upsides of the ALD process: It is possible to achieve high uniformity along the substrate, which also allows to scale up the reactor for batch processing or loading of multiple substrates for experimental work. Due to the self-limiting characteristic a highly conformal deposition is possible as well. This holds up for complex structures and surfaces with high aspect ratios, as well as scaled down processes, which are particularly important in DRAM fabrication. ALD deposition with **a**spect **r**atios (AR) of 30:1 and higher can already be achieved with oxides. Nitrides have a higher recombination probability, allowing ARs of up to 10:1. [6]

1.2 Cycles of ALD

A basic ALD process consists of four alternating cycles. Alternatively, the process can also be divided into two half cycles A and B. The process is shown in figure 1.2. The GPC dependece on the process time of the associated step can be seen on the lower part of the graph. It is assumed that the respective process times are in saturation. The saturation times are heavily dependent on the reactor volume and vary from publication to publication even for the same materials under similar conditions.

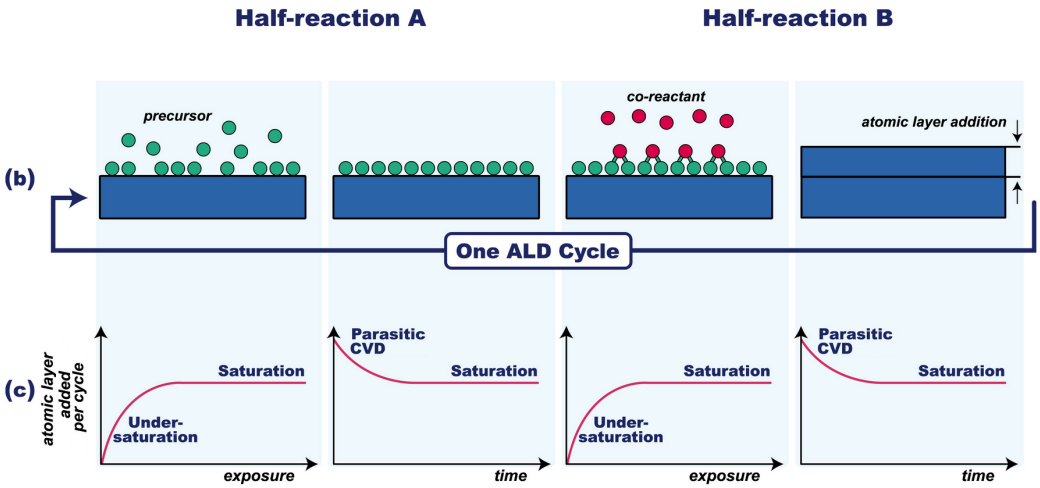

Figure 1.2: Scheme of an ALD cycle. In the second half cycle in plasma enhanced ALD the surface is exposed to plasma. In thermal ALD exposure happens with a reactant gas. Reprinted and adapted from [7]

- Precursor dose:
  The precursor valve opens, and the active sides of the molecules adsorb on the surface. If the time of this step is chosen to be too short, the substrate is not fully covered. This leads to a lower GPC as well as to a high fluctuation in thickness along the substrate, usually descending away from the inlet of the precursor dose. Furthermore, the density of the film is lower since the surface is not fully covered.
- Purge dose:
  An inert gas is used to purge the chamber and remove remaining

molecules in the reaction chamber. With this, reactions of the precursor and co-reactant off the surface can be avoided. If the purge time is chosen too low, CVD-like growth will occur. This growth is not self-limiting anymore and the GPC is increasing.

- Co-reactant or plasma dose:
  In thermal ALD the co-reactant, often a reactive gas, is pulsed in the reactor. This leads to interactions between the surface molecules from the precursor and the co-reactant. In PEALD (**p**lasma **e**nhanced ALD) the gas is pulsed in and voltage is applied to create a plasma. If the co-reactant time step is not long enough, the open sites on the surface only react partially, and the surface is not fully covered. Similar to a short precusor dose, this leads to a decrease in growth and a change in thin film characteristic.
- Purge dose:
  Similar to step two, but the plasma molecules are purged instead.

Additionally, to the basic ALD setup of two alternating cycles, more complex schemes can be used. For example in an ABC multistep process, a second co-reactant or precursor is introduced followed by a purge cycle. Different material properties like electrical and thermal conductivity can be altered with the use of a multistep process.

A cycle made up of two or possibly more cycles, each again consisting of two half-cycles, is called supercycle. It allows for multilayer deposition, doping of certain materials or a specific elemental mixture. The first cycle is run m times, then followed by the second cycle which is run n times, those m+n cycles make up one supercycle. A comparison of those process variants can be seen in figure 1.3

1.3 Temperature window of an ALD process

Since surface reactions are mainly driven by thermal energy, most ALD processes have a characteristic temperature range in which self-limiting growth is possible. Within this temperature window, the thin film characteristics and GPC are - in theory - constant and not temperature dependent. If the deposition is done outside of this temperature window, several problems

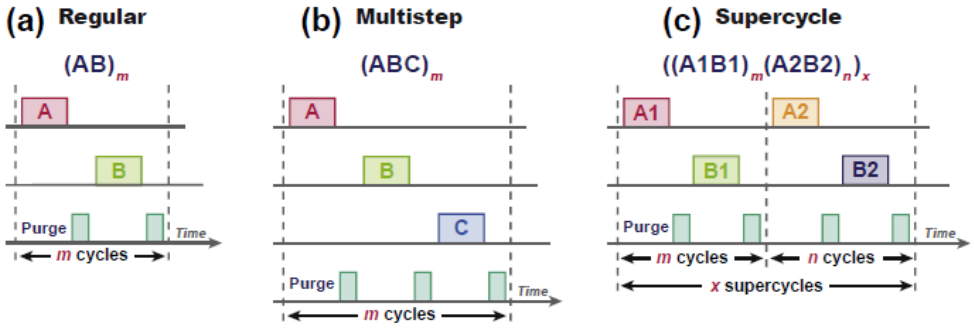

Figure 1.3: Comparison of regular cycles (a), a multistep process (b) and supercycles (c). In a multistep process additional cycles are added, whereas a supercycle consists of two or more complete cycles, which are then run m and m times, adding up to one supercycle. Reprinted from[2]

arise. At low temperatures molecules of the precursor or co-reactant including carbon residues can condensate. This will lead to an increase in GPC. The limited thermal energy can also lead to a lower GPC due to decreased thermal energies. At higher temperatures decomposition of the precursor can occur, resulting in CVD-like growth. Molecules can also desorb from the surface, decreasing the films growth rate.

These effects put an upper and lower limit to the temperature range in which ALD growth can be achieved and puts a limitation to multistep or supercycle depositions, where it is necessary for ALD windows of several process steps to overlap.

1.4 Advantages of plasma enhanced ALD

To overcome limitations like the thermal window of the conventional (thermal) ALD process and widen the variety of used materials and process techniques, plasma can be used as a co-reactant in the process. A plasma is a gas consisting of ions end free electrons with the same particle density of ions and electrons on a macroscopic scale and are therefore quasi-neutral. It is usually generated by applying an electric field to the gas to ionize the

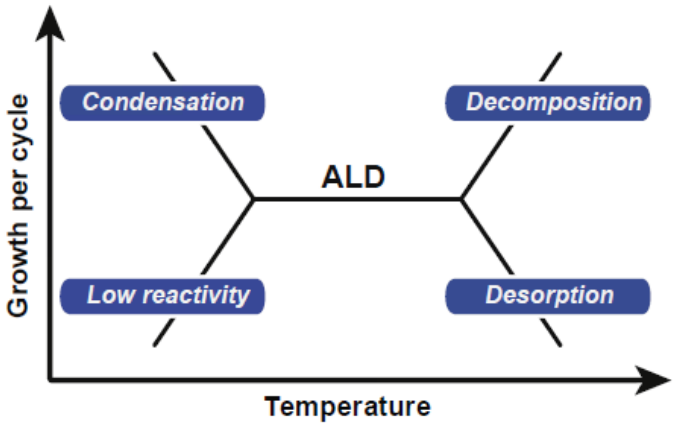

Figure 1.4: Temperature window of an idealized ALD process. Within this window the GPC and film properties are unchanged. If the temperature is too low or too high, depositions are not surface controlled and show CVD like growth. Reprinted from [2]

atoms of the used gas. Gas most used are H_2O, O_2, H_2, N_2 or NH_3 . The kinetic energy of the electrons is about 3 eV, which equals to a temperature of about 3500 K. Due to the higher mass per charge, the kinetic energy of the ions remains lower, with a temperature of about 300-500 K. The ions gas is therefore referred as cold plasma. Generating the plasma and working with PEALD has several advantages over thermal ALD:

- Deposition at reduced temperature:
  Contrary to thermal ALD, where the energy for surface reactions only stems from the thermal energy delivered by the heating system, the plasma is much more reactive due to the existence of free radicals. They are electrically accelerated towards the surface and therefore exhibit higher anergies.
- Improved control over film composition:
  The use of plasma introduces new parameters that can be changed in order to tune material properties. The plasma power, the operating pressure or the plasma exposure time can be changed. Furthermore, different gases can be mixed. When doping a material with N under O_2 plasma, the amount of nitrogen can be easily altered, since the free electrons have a very high kinetic energy and enable them to break

up the nitrogen triple-bond. While adjusting those paramaters, the plasma still has to be stable upon firing and can only be adjusted within a certain framework. This range however is rather broad and the parameters themself influence each other as well.

- Increased precursor and material choice and improved properties:
  More stable precursors and materials, even at elevated temperatures, can be used due to the high reactivity of the plasma, which would not be possible with conventional ALD since the reactivity is lower. This also allows using lesser reactive and therefore often less toxic precursors. This is often a determining factor since safety concerns play a deciding role in which chemicals can be used and which not. Depositions of titanium nitride (TiN) with plasma ALD and TDMAT (**t**etrakis-**d**i**m**ethyl-**a**mino-**t**itanium) precursor, were reported with different plasma types, as described in section 2.2.2 in further detail. Lower impurities and higher electrical conductivity were achieved by using N_2-plasma, compared to H_2O and N_2-H_2 mixture-plasma. [8]
- Increased growth rate:
  Higher reactivity not only leads to more dense films with fewer impurities, but often to higher growth rates in terms of GPC. This has also been shown in the case of TiN deposited with TDMAT, with N_2 and NH_3, each being used as plasma and thermal ALD configuration. Thin film growth was not only achieved at lower temperatures for PEALD, but also at an increased GPC for both gases with the use of plasma at same temperature was reported. [9]

1.5 Precursors and materials

Figure 1.5 shows a periodic table marked with the elements that were already deposited within the ALD process. In the early days of ALD the majority of compounds were binary, advances in process technology and increased effort, due to high demand from industry, led to an increase in deposited elements and alloys. Superalloys, compounds with complex compositions and doping concentrations, are just one of many examples.

Furthermore, the knowledge of precursors is still increasing and leads to

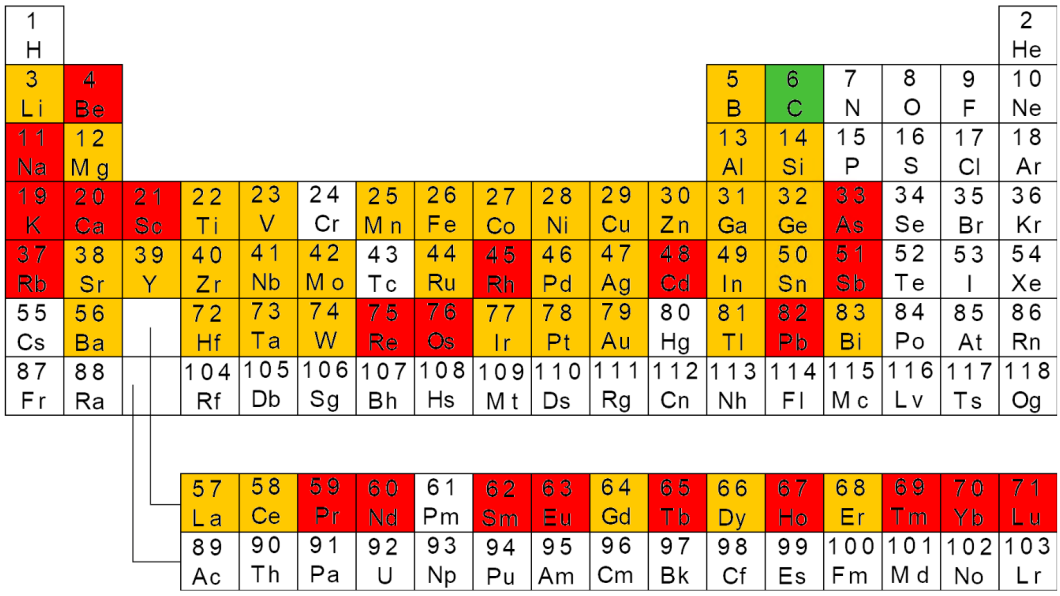

Figure 1.5: This figure shows a periodic table of deposited elements via ALD. Marked in red are elements processed with thermal ALD. Carbon, marked in green, was deposited with PEALD and for elements marked in yellow, plasma and thermal ALD depositions have been reported. This periodic table includes deposition of oxides, sulfides, nitrides, fluorides, phosphates and pure elements as of February 2019. Data taken from [10]

more possibilities of multielemental process combinations. Most prevalent are metalorganic precursors. Inorganic or elemental precursors are also in use. Contrary to a CVD process, there must be no gas phase reactions to obtain a surface controlled growth in the process. Reactions occur only on the surface in order to obtain self-limiting and surface controlled ALD growth. The precursor must be thermally stable within the temperature window of the desired ALD process. A sufficent vapor pressure above the working pressure is also required in order to pulse enough of the precursor into the chamber.

To operate the system, it is also preferable that the precursor has a low toxicity and is easy to handle. These features can often be achieved with ligands. Ligands are functional groups that bond with a central metallic atom. The organic functional groups donate the binding electrons to the metallic atom.

2 Materials

2.1 Properties of aluminum nitride

In this chapter basic mechanical, crystalline and electrical properties of aluminum nitride are explained, as well as how it was deposited via ALD so far in literature.

2.1.1 Crystal structure

Aluminum nitride is a binary electrical insulator and has a wurtzite structure, a hexagonal crystal system. Due to the asymmetry of the structure - it shows no inversion symmetry - many wurtzites, including aluminum nitride, show piezoelectric or pyroelectric properties. One of its applications are epitaxially grown films used as surface acoustic wave sensors. The lattice constants were found to be a=3,11 Å and c=4,98 Å, leading to a ratio of c/a=1,6 which slightly varies from the ideal ratio of c/a=$\sqrt{8/3}$=1,633. [11] A basic hexagonal wurtzite structure is shown in figure 2.1 .

2.1.2 Optical properties

The bandgap of AlN was reported in several publications to be in the region of just below 6 eV. Chen et al. measured a band gap of 5,95 eV grown with reactive sputtering. [12] The wide bandgap makes it interesting for research in LEDs operating in the UV regime, with wavelengths of 230 nm and below in combination with GaN. [13] The optical properties of AlN thin films can be modeled with a Cauchy-Urbach-Model,which is suited for optically

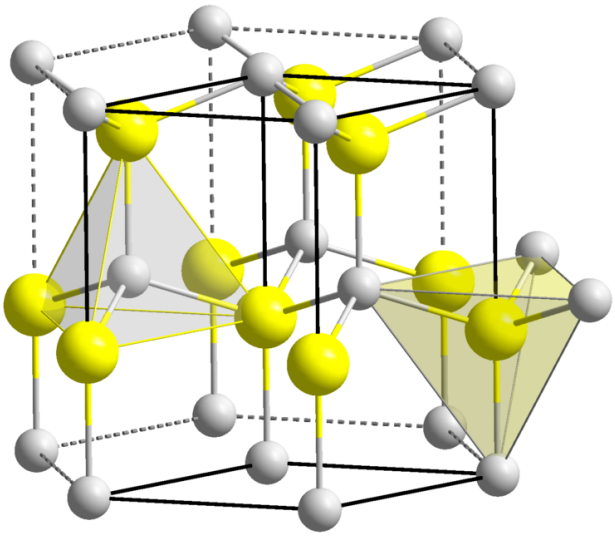

Figure 2.1: Picture a wurtzite structure. Each type of atoms forms a hexagonal close packed sublattice itself.

transparent materials. The refractive index and extinction coefficient can be modeled accordingly:

$$n(\lambda) = A + \frac{B}{\lambda^2} + \frac{C}{\lambda^4} \tag{2.1}$$

$$\kappa(\lambda) = \alpha * exp[\beta(12400(\frac{1}{\lambda} - \frac{1}{\gamma}))] \tag{2.2}$$

Where λ is the wavelength in nm, κ is the extinction coefficient, A, B, C, α and β are variable model parameters and γ is the band edge. The non-cubic structure leads to anisotropic optical properties, causing a change of refractive index dependent on the orientation. Reactive sputtering experiments done by Ababneh et al. [14] show a correlation of refractive index and peak count of the c-axis orientation XRD peak with the refractive index varying between 1,9 and 2,15 at 543 nm, indicating anisotropic behavior. The film thicknesses were between 400 and 500 nm, the data can be seen in figure 2.2

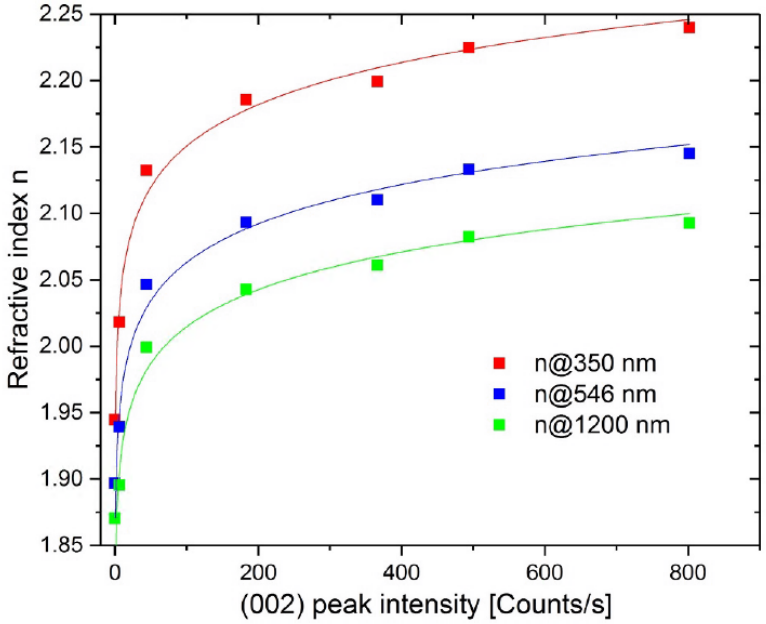

Figure 2.2: Refractive indices of AlN at three different wavelengths depending on the peak intensity of the (002) peak, corresponding to the intensity of c-axis orientation. Reprinted from [14]

2.1.3 PEALD of Aluminum nitride

Articles have been published for AlN depositions with **t**ri-**m**ethyl-**a**luminum (TMA) and either N_2-H_2 or NH_3 plasma. Since hydrogen is highly flammable and even small leakages can cause a Knallgas-explosion and ammonia is highly toxic, N_2 plasma was used in this thesis, which also has been shown to be a viable choice for deposition of TiN films.

Alevli et al. [15] conducted AlN depositions with TMA and ammonia plasma in a remote configuration at 300 W. With a recipe of (40/10/0,1/10) s (plasma time/plasma purge/precursor exposure/precursor purge) about 100 nm AlN were deposited at different temperatures. An ALD window of self limiting growth was found between 100 and 225 °C and saturated at 0,9 Å per cycle. Above 225 °C the growth per cycle is increasing linearly at a temperature up to 1,5 Å at 500 °C and an increasing density from 2,65 to

about 2,96 g/cm^3 was measured. The refractive index at 533 nm modelled via ellipsometry measurements was increasing from 1,88 to 2,08 as well.

Perros et al. [16] compared AlN depositions done with ammonia and N_2-H_2 plasma. The experiments were performed with a remote plasma set-up and a power of 80 W, the plasma time was 20 s. The base pressure was kept at around 1 mbar at 200 °C and a TMA pulse time of 400 ms was chosen. With ammonia, a density of 2,56 g/cm^3, a refractive index of 1,90 and a GPC of 0,89 Å was achieved, matching the findings of Alevli et al. [15]very well. Depositions with a nitrogen-hydrogen mix-plasma are denser by a small amount with a refractive index of 1,92 and a densitiy of 2,65 g/cm^3. The GPC was reduced to 0,61 Å.

Fourier-**t**ransform **i**nfra**r**ed pectroscopy (FTIR) showed N-H, C-N, N-H, and C-H bonds besides the desired bonding of Al-N for both plasma types. Composition analysis with time-of-flight **e**lastic **r**ecoil **d**etection **a**nalysis (ERDA) has shown a smilar composition of around 42 at. % N, 35 at. % Al and 21 at. % H. Carbon impurities were 1,4 at. % for the ammonia plasma and 1,2 at. % for the mixed plasma respectively.

A study done by Bosund et al. [17] with ammonia plasma showed a linear increase of the growth rate with the temperature from 0,73 to 1,32 Å between 100 and 300 °C per cycle, leading to a GPC of 1,02 Å at 200 °C. The roughness also increased from 0,7 to 2,8 nm within the temperature range. At 100 °C, the oxygen concentration was increased to over 35 at. %, and dropping to under 1 at. % at higher temperatures. Film deposition is not stable below 150 °C. Hydrogen concentration dropped linearly from 27 to 13 at. % from 300 to 150 °C, carbon impurities were at about 2-3 at. % over the whole temperature range.

The refractive index increased from 1,84 to 1,98 from 150 to 300 °C at 633 nm and the mass density also increased from 2,34 to about 2,8 g/cm^3 within the same temperature range. Roughness went up from about 1,0 to 2,8 nm as well. While lower temperature films showed no crystallinity, at 300 °C the (002) peak appeared up in XRD spectra.

TMA saturation was found to be 200 ms and plasma saturation time 15 s. Purge times are not mentioned in the article. The dependence on film thickness was studied for the plasma time as well at 60, 80 and 100 W of

plasma power. An increase of thickness variation was observed for plasma times clearly below the saturation time, as well as for increasing plasma times of 20 s or higher at 100 W. This indicates that the plasma is starting to damage the sample. A plasma power of 100 W leads to about 10 % increase in GPC compared to 60 W with a direct plasma setup.

2.2 Properties of titanium nitride

In this chapter basic mechanical, crystalline and electrical properties of titanium nitride are explained, as well as how titanium nitride is deposited via ALD. Titanium nitride has typically a face centered cubic crystal structure [18] of NaCl-Type. This means that each titanium atom is surrounded by six nitrogen atoms and vice versa in bulk material, leading to a 1:1 stoichiometry. [18]

2.2.1 Opto-electrical and mechanical properties

TiN shows excellent mechanical properties and is often used as hard coating for drills and cutting tools. Its use is most prevalent as coating for stainless steel, increasing the steels corrosion resistance and hardness. A study done by Chou, Yu, and Huang [19] with reactive sputtering showed that the hardness of the TiN coating is increasing from 15 GPa at 200 nm to 35 GPa at 800 nm. Within the same range also the internal stress decreased from -5,9 GPa to about -3 GPa. [19]

TiN deposited with atomic layer deposition finds is used as a diffusion barrier in integrated circuits. Combining low resistivity and high thermal stability (with a melting point of 2950 °C), TiN meets the semiconductor's industry requirement. In DRAM (dynamic random access memory) [20] manufacturing, where it is necessary to deposit structures of high aspect ratios, it is used as diffusion barrier.

As a transition metal-nitride, TiN also exhibits a very high conductivity and shows superconductivity below the critical temperature of 6 K. At very low temperatures TiN is a superinsulator. It therefore shows absolutely no

conductivity below the critical temperature and exhibits opposite effects of a superconductor. The transition temperature has been found to lie within 20 - 70 mK. [21]

The optical properties are best described by a Drude-Lorentz model, in which the electrons are damped harmonical oscillators. The intraband transitions are described by the free electron model (Drude part). It assumes a free electron gas with an external field pulling electrons to one side and collisions with lattice ions at random angle. Transitions between different bands can be described with Lorentz oscillations. A further detailed description can be found in chapter 3 of *The Physics of Solids* [22].

Patsalas and Logothetidis [23] were able to model 100 nm thick, reactive sputtered films that are in good agreement with the experimental data. A single Drude term and two Lorentz oscillators and a maximum plasma energy of about 7,7 eV were used. This means that only photons above this energy - which equals a wavelength of 171 nm - are transmitted, whereas visible light is reflected out at 400 °C. The mass density was estimated to be 5,7 g/cm^3 with both ellipsometry and X-ray reflectivity. [23]

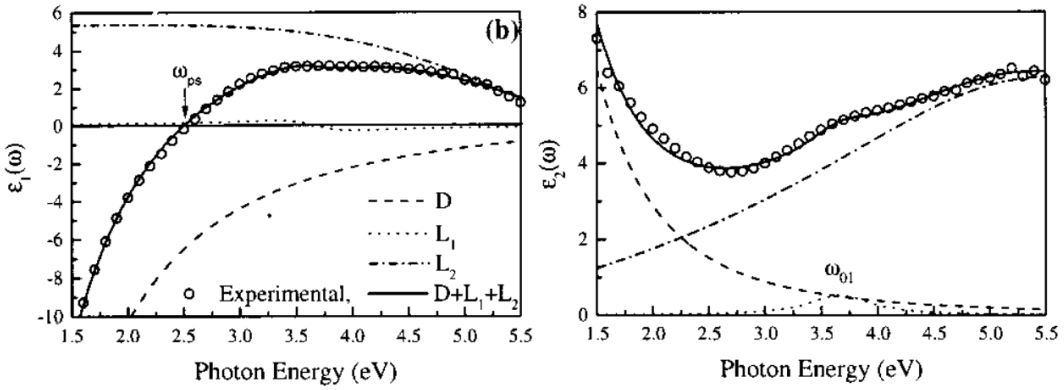

Figure 2.3: Real (left) and imaginary (right) part of the dielectric function of reactive sputtered TiN films at room temperature and a bias voltage of -120 V. The experimental data is marked in small circles, whereas the single contribution of the Lorentzian and Drude terms are dashed. [23]

2.2.2 PEALD of titanium nitride

Studies on titanium nitride have been conducted with either TDMAT (**T**etrakis-**dim**ethyl**a**mino-**t**itan) or $TiCl_4$ on both thermal ALD and PEALD. In PEALD, both ammonia and nitrogen plasma have been used. As mentioned in chapter 2.1.3, N_2 plasma was planned to be used for TiN depositions. As a precursor, TDMAT was chosen due to the high reactivity and toxicity of hydrogen-chloride which is formed upon reaction with $TiCl_4$.

Musschoot et al. [24] used a total cycle time of 25 s, with (6/8/2/9) s (co-reactant or plasma time/plasma purge/precursor exposure/precursor purge), for plasma as well as thermal ALD. In case of PEALD the 300 W indirect plasma power source was switched on for five seconds. In this study both N_2 and NH_3 were used as co-reactants. Depositions done with nitrogen showed a minimum growth per cycle at 150 °C at about 0,5 Å per cycle, increasing up to 0,8 Å for as low as 50 °C and up to 4 Å per cycle at 350 °C. No deposition was achieved below 250 °C for thermal ALD.

The thickness dependence on the precursor exposure time did not achieve ideal saturation with ammonia plasma, which is lining up with results from Krylov et al. [25], where no saturation was found for TiN films deposited with NH_3 as well.

The resistivity of TiN thin films deposited with ammonia plasma dropped significantly from 3700 down to 800 $\mu\Omega$cm with increasing plasma power between 100 and 500 W. With a higher plasma time, the resistivity could be further decreased to under 300 $\mu\Omega$cm. XPS measurements showed a shift of the C1s peak, indicating titanium carbide formation in thermal ALD depositions done with ammonia. Furthermore, binding energies for TiO_2, Ti_2O_3 and TiC/TiN bonding energies were detected on the surface, indicating oxidation of thermal ALD films. Both these peak profiles could not be found on films deposited with plasma ALD. [24]

Remote plasma depositions with TDMAT as precursor heated at 45 °C and three different types of plasma - N_2, H_2 and N_2-H_2-mixture were studied by Kim et al. [26]. The process times were (20/5/5/5) s and the working pressure was kept at 100 mTorr and the plasma power was fixed at 300 W. A typical ALD window was found for all three plasma types within

a temperature range from 200 to 300 °C. Below 200 °C the growth per cycle dropped, whereas a growth increase was reported above the thermal window. The growth per cycle within the ALD window was about 0,34 Å per cycle for each plasma.

A drastic difference could be seen in the resistivity, which was lowest for pure N_2 plasma at about 300 $\mu\Omega$cm. With hydrogen plasma, a resistivity of 600 $\mu\Omega$cm was achieved, and the plasma mixture film showed even higher resistivity at 700 $\mu\Omega$cm. Auger electron depth profiling showed a lower carbon and oxygen impurity content for the nitrogen treated films as low as 4 at. % compared to 15 at. % carbon atoms. This is likely caused by the activated nitrogen breaking the bonds between the ligand and titanium. [26]

2.3 Aluminum titanium nitride

Titanium nitride films tend to form TiO within the thermal ALD process, as mentioned in the previous chapter, but at generally higher temperatures the thin films tend to oxidize. While the oxidation starts at about 500 °C, for FRAM (**f**errolectric **r**andom **a**ccess **m**emory) devices, proccess temperatures of up to 700 °C are necessary. To overcome this problem, Lee and Kang [27] deposited Ti-Al-N supercycles with TDMAT, TMA and ammonia for the titanium films and hydrogen plasma for the aluminum films. The cycle times were (5/15/10/15) s for the TDMAT cycle, starting with the co-reactant. After that, the films were exposed to hydrogen plasma to improve the thin film quality. The step to deposit the AlN had a cycle time of (5/15/10/5) s and was pulsed in alternately.

The plasma power was kept at 200 W and the pressure at 133 Pa ($\triangleq$ 1000 mTorr) at a temperature of 180 °C. Within the saturation regime, a growth of about 0,35 nm per supercycle could be achieved and no onset growth was reported. The film showed good homogeneity with a root-mean-square deviation of 0,332 nm at 25 nm total thickness. The films had a resistivity of 500 $\mu\Omega$cm at 100 nm thickness, which is relatively high, but probably caused by carbon and hydrogen impurities. Both a 50 nm thick Ti-Al-N and Ti-N film were annealed at 700 °C for 30 minutes and the composition was

determined via auger electron sputtering. It could be shown that for AlTiN films the oxygen concentration dropped from 35 at. %. to below 5 at. % compared to TiN films, showing increased oxidation resistance for AlTiN films. [27]

A patent filed by Fujita, Tanaka, and Nagaotomo [28] describes thin films with various elemental compositions obtained reactive sputtering, in order to produce metal nitride negative coefficient thermistors (NTC) with high conductivity and heat resistance.

In case of Al based films either titanium or chromium doping was used. The Al films are oxi-nitrides with a N:O ratio of at least 65 at. % nitrogen. It has been found that for higher oxygen concentrations the wurtzite phase could not be obtained anymore, leading to decreased heat resistance and a lower B value. The atomic ratio of Ti:Al must be somewhere in the region between 0,3:0,7 and 0,05:0,95. If the films are too heavily doped with titanium atoms, the wurtzite structure - which gives the films their NTC behavior and high heat resistance - is lost and replaced by a Na-Cl-type phase. In case of a low titanium concentration, the films show high electrical resistance and are therefore not suitable to be used as a thermistor. [28]

A paper published by Yun et al. [29] was one of the few exceptions using N_2 plasma only for depositions of AlTiN. TDMAT and TMA were in use as precursors. The cycle time was set to (20/10/1/10) s for the TiN subcycle and (10/10/1/10) s for the AlN cycle respectively. The plasma was operated at 300 W and the temperature of the TDMAT precursor was kept at 35 °C at a working pressure of 3 Torr. Under these conditions a growth per cycle of 0,1 nm for pure AlN films and 0,05 nm for pure TiN films at 200 °C was achieved.

EDX analysis for different ratios of Al to Ti cycles showed that films consisted of a $Ti_{0,25}Al_{0,25}N_{0,5}$ stoichiometry, if one supercycle was made up of 10 TDMAT cycles followed up by 1 cycle with a TMA pulse. The expected combined growth rate of 0,62 nm was not quite achieved with a total growth of 0,5 nm, indicating a lower reactivity and reaction rate of the TDMAT precursor on the AlN surface. XRD measurements showed no crystallinity for the AlN films, whereas the TiN (200) peak was much less prominent in the mixed film compared to pure TiN at 20 nm film thickness.

The surface roughness for 50 nm thick films improved significantly from 1,33 nm for the TiN films to 0,76 nm for the transition metal nitride film. However the conductivity was very high at 2800 $\mu\Omega$cm, compared to 475 $\mu\Omega$cm of pure TiN films, both being about 20 nm thick.[29] No determination has been done in terms of film composition of the AlN films and very few information on AlN films deposited with nitrogen plasma has been published yet.

3 Characterization

In this chapter an introduction to the methods used to chracterize the deposited thin films is given. With these methods one is able to determine thin film properties like composition, thickness, optical constants and crystallinity of the grown Al(Ti)N films.

3.1 Fourier transform infrared spectroscopy (FTIR)

Absorption spectroscopy measures the absorption of radiation after interaction with a sample. The energy of IR (infrared) light lies within the energy range of stretching and bending of intramolecular bondings. Excitations due to radiated photons appear at characteristic energy values. Due to the quantum mechanical nature, those energies are discrete, and therefore a specific feature in the spectrum allows for identification of a certain bond. It is however not always possible to assign every feature in a spectrum and overlapping features also leave space for interpretation. [30]

While monochromatic light is required at multiple wavelengths to obtain a full spectrum in the described process above, which is very time consuming, in FTIR a broadband light source is used in combination with a Michelson interferometer to obtain information rapidly. A basic setup can be seen in figure 3.1.

For the IR light source, a Globar is used which is a silicon carbide rod heated up to over 1000 °C for photon generation. After the beam is focused with various lenses, the light enters a beam splitter, usually a half transparent mirror, and each of the beams is then reflected from the two mirrors, with

one of them being adjustable. The beam recombines again at the beam splitter, interacts with the sample before it enters the detector, where the interferogram is then measured. The path difference (2x) can be adjusted by moving the mirror back and forth. If the path difference is an integer number of the wavelength, it comes to constructive interference and light will pass through the detector, thus the intensity can be measured. Therefore, one can obtain the IR spectrum as a function of mirror position, the interferogram. In order to obtain the spectrum, which is the intensity dependent on the wavelength, the signal needs to be Fourier-transformed by the computer and the emitted radiation of the source can be measured. When the sample is now put in the light path, the absorption spectrum can be measured and with division by the reference, an absorption spectrum can be obtained. [30]

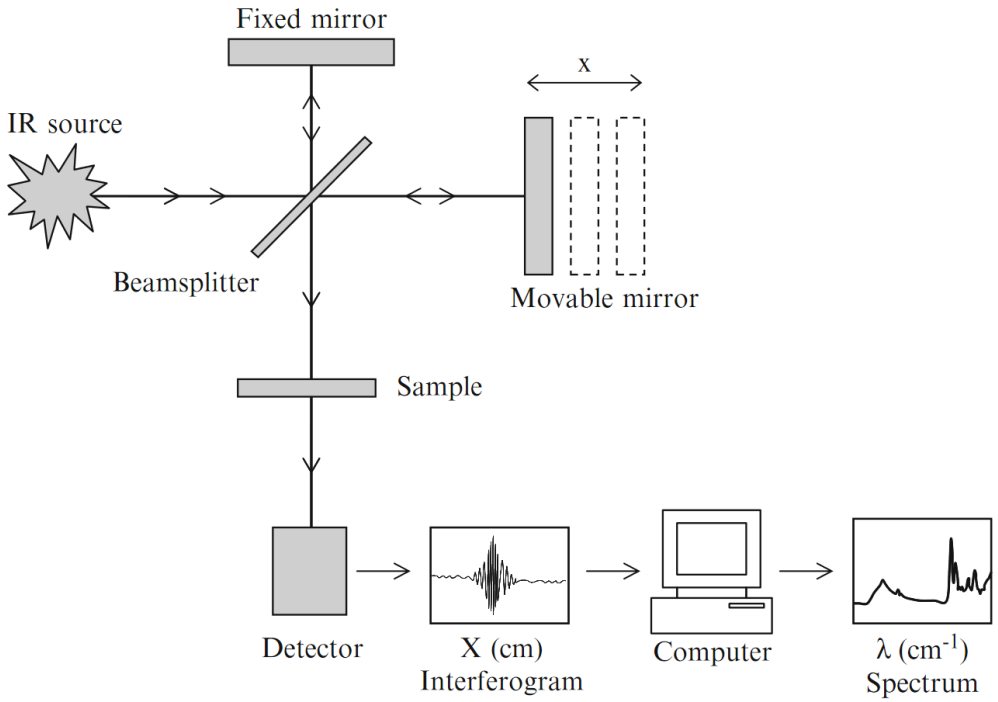

Figure 3.1: Setup of a FTIR including the IR source, Michelson interferometer, detector and the computer for Fourier transformation. Reprinted from [31]

3.2 Spectroscopic ellipsometry

Spectroscopic ellipsometry is an indirect method to determine the optical constants, the refractive index n and the extinction coefficient k, as well as the film thickness of grown thin films. Polychromatic linearly polarized light is shone on a surface and interacts with the thin film and substrate. The electromagnetic waves change in amplitude ratio and a phase shift of the s- and p- polarized light can be measured.[32]

The basic working principle can be seen in figure 3.2. For measurements a J.A. Woollam Co M-2000V ellipsometer was used. It was operating at a wavelength from 371 to 1000 nm and measurements were done at incident angles of 60, 65, 70, and 75 °. The change in polarization is given with the phase difference Δ and ratio of the amplitude Ψ. The subscripts i and r represent the incident and reflected light, while p and s are labels for the polarization directions.

$$tan(\Psi) * e^{i\Delta} = \frac{\frac{E_{rp}}{E_{ip}}}{\frac{E_{rs}}{E_{is}}} = \frac{r_p}{r_s} \tag{3.1}$$

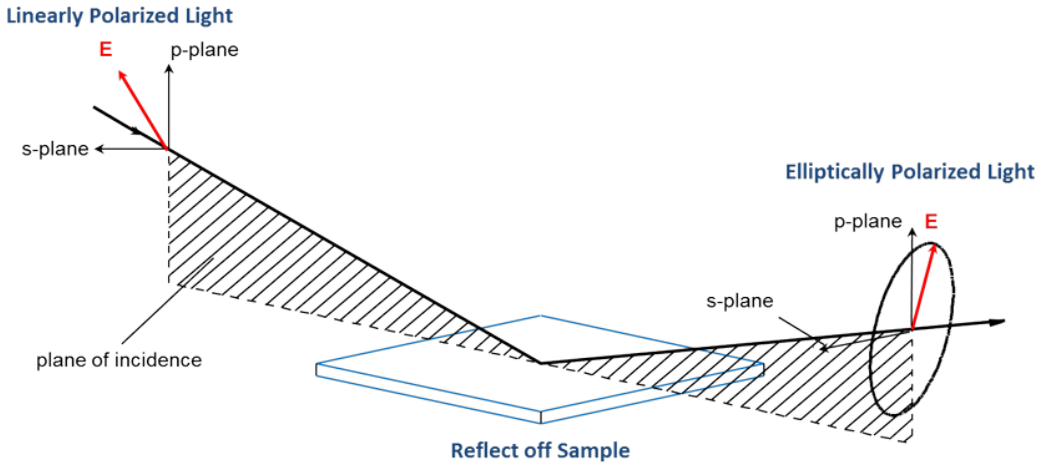

Figure 3.2: Working principle of a spectroscopic ellipsometry measurement. Reprinted from[32]

When light interacts with matter, it reflects according to the Fresnel equations in order to satisfy the Maxwell equations. This leads to boundary conditions at the interface which must be satisfied. They are different for s- and p-polarized light. At each interface between two materials, with a change in the refractive index, it can result in both transmission and reflection of the beam. For transparent and very thin films it will come to multiple reflections on the surface as well as reflections at the interface between substrate and thin film leading to superposition of multiple electromagnetic waves. A sketch of this can be seen in figure 3.3 [32]

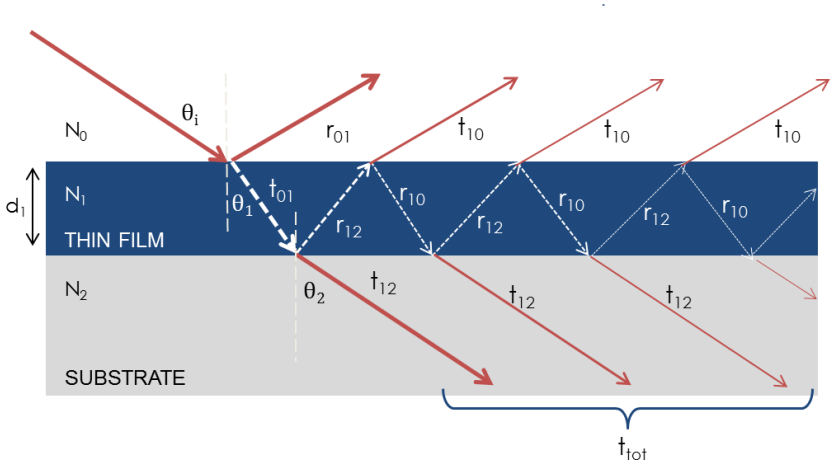

Figure 3.3: Optical path of a single layer thin film on a substrate. Adapted from [32]

After the sample is measured and a model is constructed, it is then simulated within the CompleteEASE software. The experimental data of the measured intensity of the p- and s-polarized light is then compared to the optical model. In this case, the model consists of a silicon substrate wafer and an 1,6 nm silicon oxide layer additionaly to the grown layer, however the parameters for the substrate and oxide layer are fixed. It is then compared to the experimental data with an initial guess of the optical model and the unknown parameters are varied until the MSE (mean squared error) is minimized. Typically for optimization problems, it can happen that the found minima is not a global, but only a local one, depending on the starting values which are put in. This issue occurs mostly when analyzing thin films below 5 nm, where the minima are very broad and shallow.

3.3 X-ray diffraction (XRD)

X-ray diffraction is a characterization technique that allows for determination of the crystalline structure of the thin film. In specular XRD, monochromatic x-rays are radiated on the sample and the beam is elastically scattered at an entrance angle θ, meaning the entrance and the exit angle are the same regarding the surface normal vector. Reflections occur not only topmost plane of the crystal but can occur on underlying planes as well. If Bragg's Law (equation 3.2) is fulfilled, the path difference of two diffracted beams is equal to the wavelength of the x-ray radiation - which is the wavelength of Cu-kα radiation at 1,5404 Å - a spike in intensity can be observed. A geometric sketch is drawn in figure 3.4.

$$2 * d * \sin\theta = \lambda \tag{3.2}$$

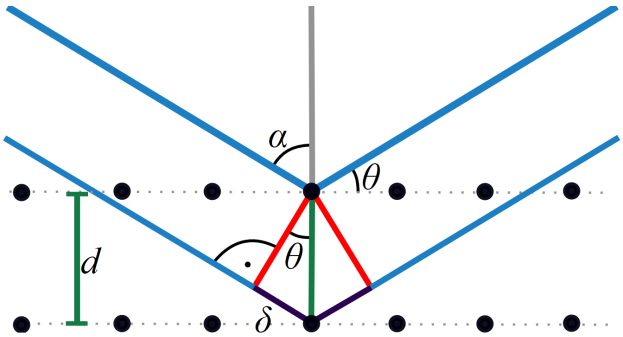

Figure 3.4: Working principle of an XRD measurement, with the incident angle θ, the interplanar spacing d and the path difference δ

In order to measure over a certain range of angles, usually a $\theta\backslash 2\theta$ scan is performed. This means that the entrance angle θ is varied and the angle between diffracted and incident beam is 2θ over the whole scan. With this scan mode, the distance of lattice planes parallel to the surface are contributing to the peak intensity. While the peak height (estimated by the peak count minus the background) can be used to determine relative intensities - for example two samples were prepared under different conditions and show different relative peak heights, the full width at half maximum (FWHM)

of the peak allows for determination of the crystalline grain size. [33] For measurements a Malvern Panalytical Empyrean diffractometer was used.

3.4 X-ray reflectivity (XRR)

XRR uses the same experimental setup as XRD, however thin films are investigated at low angles, usually below 5 °. It allows for determination of the roughness, thickness and refractive index in the x-ray regime, which gives information about the electron density and subsequently the mass of the thin film. Contrary to XRD, it does not use diffraction effects but makes use of multiple reflections within the sample and measures the intensity depending on the incident angle. Also this allows for investigation of amorphous samples. [34]

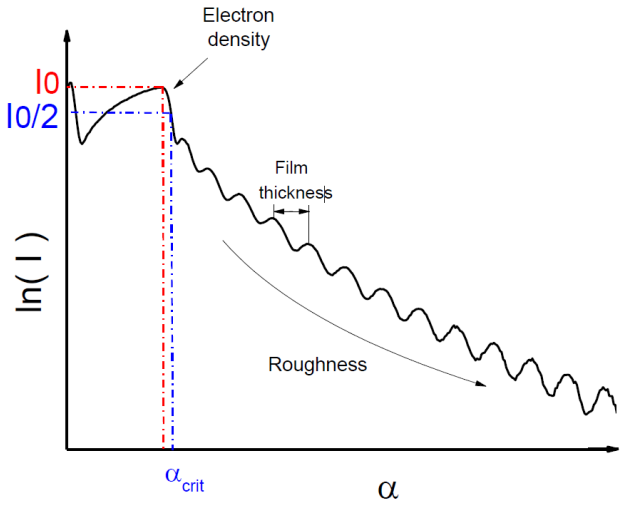

Figure 3.5: Example spectra of an XRR measurement. Reprinted from [35]

An example spectra of an XRR measurement can be seen in figure 3.5. The first prominent feature, which allows for determination of the electron density is the critical angle α_{crit}. Total internal reflection below the critical angle appears because the refractive index in materials is usually just below one and therefore below the refractive index of air in the regime of x-rays.

For low angles the X-ray beam cannot enter the thin film and therefore gets reflected out.

The refractive index n is given by following equation:

$$n = 1 - \delta + i\beta \tag{3.3}$$

with the dispersive part being

$$\delta = \frac{\lambda^2}{4\pi} r_e * \rho_e \tag{3.4}$$

Where r_e is the classical electron radius, ρ_e the electron density of the solid. Putting the latter equation in the upper one it can bee seen that the refractive index - and therefore the angle of total internal refraction - is dependent on the electron density, which then can give conclusions about the mass density with prior knowledge of the thin film. This can be of use, if the film composition is known, but the mass density is not determined due to porosities or different degrees of crystallinity. [36]

For angles larger than α_{crit} the x-rays two things can happen upon penetration into the surface: either the reflect further into the substrate, where they no signal can be picked up at the detector, or undergo one or possibly multiple reflections between the air-film or film-substrate interface. This is similar to reflections of photons in ellipsometry. A sketch of this can be seen in figure 3.6. As with XRD measurements, it comes to constructive interference, if the optical path difference is equal to a multiple integer number of the wavelength, leading to an increase of signal intensity. Those features are called Kissing fringes and appear at a certain periodicity with a change in incident angle. The angular spacing between the fringes is directly related to the film thickness, with thicker films showing more change in optical wavelength upon change in incident angle and therefore show up more frequently. [34]

The last film property, that can be measured with XRR is the roughness. The roughness between air and thin film, called surface roughness, can be determined by the general drop in intensity with increasing incident angle. Reflections on rougher films tend to be more diffuse, which are then not

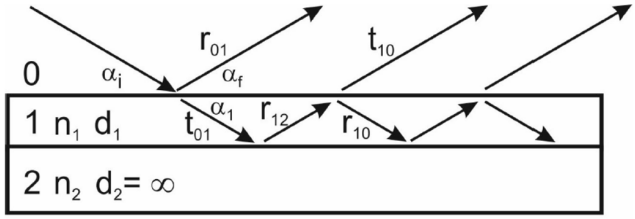

Figure 3.6: Multiple reflections of X-ray radiation on a thin film and its substrate [37]

detected and lead to a decrease in intensity. It is not shown in figure 3.6, but the interface roughness can also be determined. This not only includes the roughness between substrate and a single homogenous thin film layer, but also interfaces of multilayer systems. The electron density then gradually changes between two materials, leading to a decrease in amplitude of the Kissing fringes. [36]

4 Setup and experimental methods

This part of the thesis explains the soft- and hardware configuration of the experimental setup used to deposit thin films and a chronological description of the experiments conducted is given.

4.1 Experimental setup

A sketch of the experimental buildup can be seen in figure 4.1. In the following chapter the basic setup is explained in more detail as well as the experimental procedure.

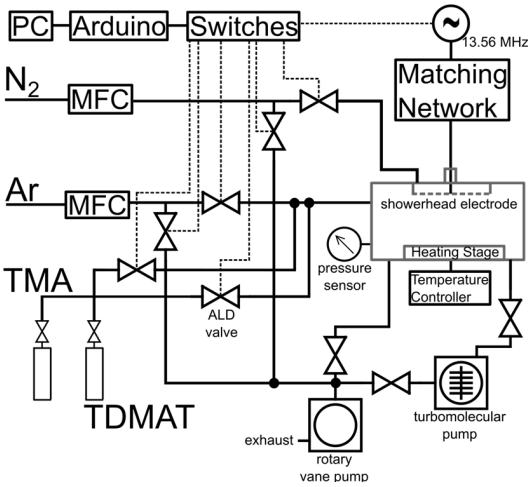

Figure 4.1: Schematic setup of the reactor. The dashed lines indicate electrical transmission lines

In order to obtain ALD like growth as described in the first chapter, it is necessary to control the gas flows as well the plasma for each cycle. This control system is realized with an Arduino, which is connected to a PC. The first part of the experimental work included a complete rebuild of all the gas lines, since they were clogged from prior depositions. Within this, the system was arranged differently within the lab in order to shorten the line distances between ALD valve and reactor as well as improve the usability of the whole system.

4.1.1 Pumping system, gas lines and ALD valve

The gas lines are 1/4 inch in diameter and made out of stainless steel. The gas flows for both nitrogen and argon can be adjusted within the mass flow controller for their gas flow factor and are both set to 20 sccm (standard cubic centimeters per minute). In order to obtain a sufficent speed to start or stop the gas flow, two magnetic valves are used as switches. While one of the gas lines is connected to the reactor, a second one is connected directly to the pump. The gas flow in the mass flow controller cannot be adjusted within software in use. Therefore, if the magnetic valve is closed, the pressure in front of the magnetic valves would build up and then being realeased upon opening. In order to avoid the pressure building up, a second line is directly attached to the pump, allowing for a constant gas flow, and preventing overpressure relative to rest of the system. This means, that either one of the lines is open during the deposition process.

While both gases have the same bypass flow, N_2 and Ar are introduced into the reactor at two separate entry points. Argon acts as carrier gas for the precursors and comes in from the side panel, while the nitrogen is flown in from the top in order to avoid a stream and increase the conformality during the plasma step. A picture of the reactor can be seen in figure 4.2. The gas line from the ALD valves to reactor are heated to avoid condensation on the lines, which caused the prior plugging within the system. The temperature was kept either at 40 °C for depositions with the aluminum precursor or at 50 °C for titanium depositions.

The pumping system of the reactor consists of two pumps. First, a rotary

Device	Company - Model
Arduino	Arduino - Mega 2560
ALD valve	Swagelok - ALD 316L
Heating cable	Winkler -
Heating controller	Omega - MCS3 2110 K-R
Manual valve	
Mass flow controller	MKS - MF1-C
Matching network	Advanced - Energy Navio
Multi gas controller	MKS - 647C
Precursor bottle heating	custom-built
Pressure gauge	MKS- Baratron
RF power generator	Advanced Energy - Cesar 13.560 MHz
Rotary vane pump	Pfeiffer Vacuum - DUO 5M
Turbo molecular pump	Pfeiffer Vacuum - TMH071P5M

Table 4.1: Devices and instruments used for the reactor setup

vane pump which is in continuous operation, is used to create a pre-vacuum. It is always connected to the reactor unless the reactor itself is opened to swap samples. Prior to the deposition the valve to the turbomolecular pump is opened and the chamber is evacuated. The turbomolecular pump is working at a frequency of 1500 Hz and the exhaust air is then pumped by the rotary vane pump. During deposition the manual valve is partly closed which creates a deliberate bottleneck in order to obtain the desired operating pressure within the reactor without having to decrease the operating frequency of the turbomolecular pump.

As shortly described in section 2, the precursors in use are TMA (tri-methyl-alumium, also $(CH_3)3Al$) to deposit AlN and TDMAT (Tetrakis-dimethyl-amino-titan, also $(CH_3)_2N)_4Ti$). Due to the high reactivity, they are controlled with special ALD valves, which offer high chemical compatibility, a fast switching time of 5 ms and airtight sealing. The valves open pneumatically and are controlled by the Arduino as well. [38]

The vapor pressure of TDMAT is rather low, about 150 mT at 25 °C [39] and therefore only barely above the working pressure of 100 mT. A heater for the TDMAT precursor bottle was therefore built and installed to increase the vapor pressure. The bottle was heated up to 50 °C at which it has a

vapor pressure of 600 mT. In comparison, TMA exhibits a vapor pressure of 2886 mT at 25 °C. [40]

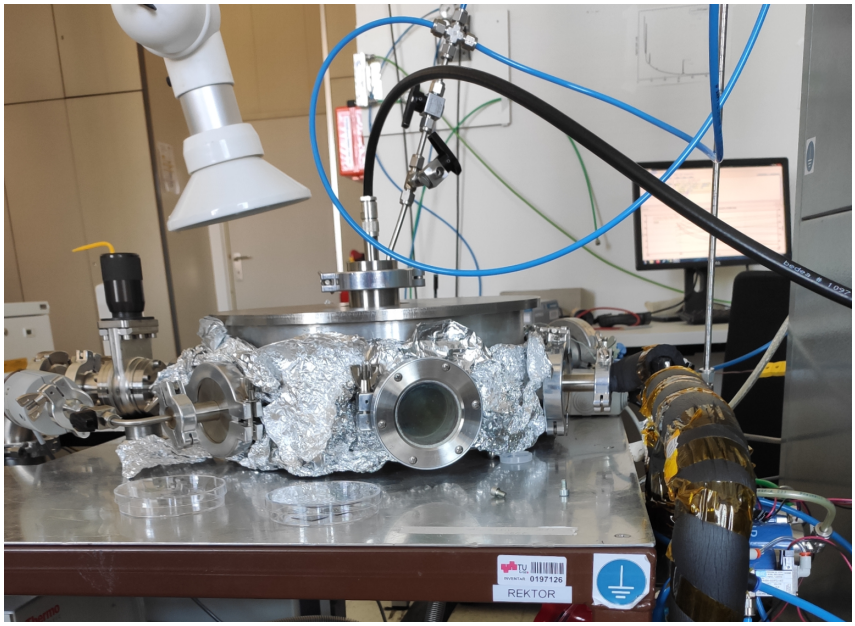

Figure 4.2: Photograph of the reactor. The plasma is fed into the reactor via the black coaxial cable. The nitrogen is introduced from the top (blue gas line). The precursor valve can be seen on the bottom right in blue. The pressure gauge is attached left of the window. The argon flows also acts as carrier gas for the precursor, the line is heated and insulated on the right side.

The heater consists of an aluminum container filled with silicon oil and two temperature controllers. The container is heated from the bottom and uses a magnetic stirrer for proper convection. Due to the exponential increase of the vapor pressure with temperature and high reactivity of the precursors, it is of great importance to make the heating system redundant. The heating controllers use magnetic relais to control the current flowing through and those tend to fail after a certain amount of switch cycles. In order to eliminate malfunctions and overheating due to a broken magnetic relais, a second heating controller has been installed in series and the oil is only heated if both heating controllers fall below a certain temperature setpoint.

4.1.2 Reactor and plasma working principle

The reactor itself is a custom-built direct plasma ALD reactor containing a heating stage inside, which can heat up to about 250 °C. Relais modules are interposed between the plasma network and Arduino and used to turn the plasma on and off. Two relais are used in order to ensure galvanic separation. They are also turned off during the plasma step to avoid interferences, since the plasma induces a high ion flux and is conductive, which then would lead to short circuits within the system.

On the outside of the system an impedance matching network is installed to avoid impedances of the radio frequency (13.56 MHz) current put in the chamber to create the plasma. The detachable top lid of the reactor acts as top electrode, while the bottom, where the heating stage is placed on, is the ground electrode. To improve conformality and uniformity within the chamber, an additional metallic ring is put between the top hat and the rest of the reactor to increase the distance between the sample stage and the plasma anode.

4.2 Software

While the hardware of the process is controlled with the Arduino, the input for the Arduino can be changed via the USB connection on the computer. It consists of a custom build software called ALD-MLD controller, which was written in phyton and has a graphical user interface. In figure 4.3 the process flow of a deposition can be seen. The whole process can contain up to 7 subsequences, written in capital letters, with each of them allowing up to 12 commands per line. Within those commands, three different types of commands followed by a number, exist: Either wait (“w5” i.e,, it is holding the current state for five seconds), open (“07” i.e., line seven is opened), or close (“c7” i.e, line seven is closed). Besides the automated process when the process is running, each port can be opened and closed manually, which is necessary in order to adjust the working pressure before the start of a deposition or for testing purposes.

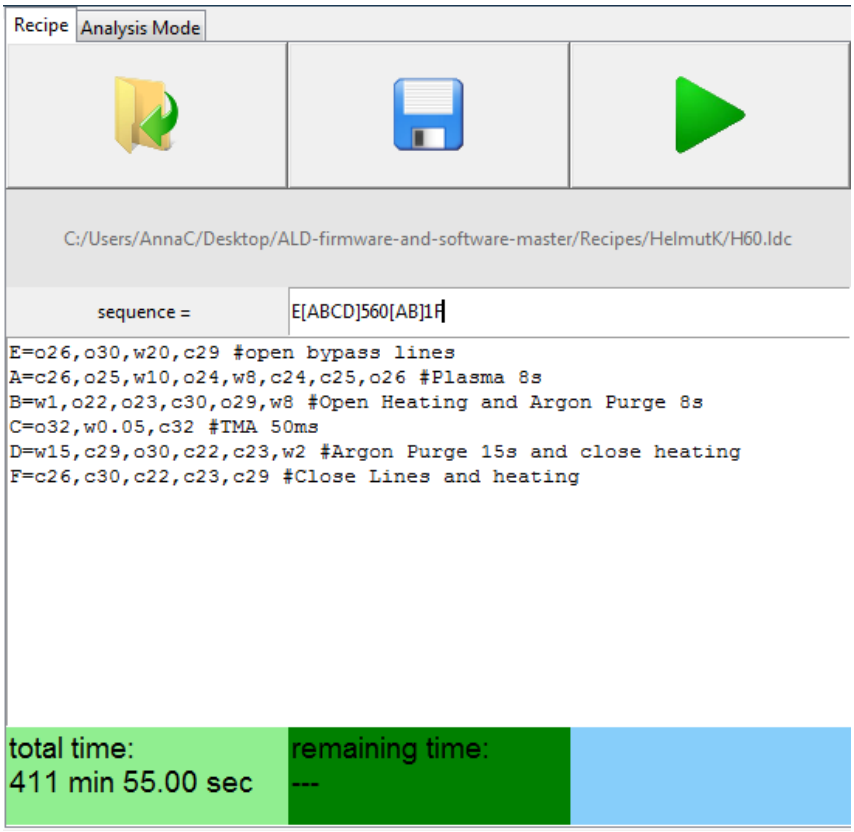

Figure 4.3: Screenshot of a deposition sequence. The port configuration can be seen in table 4.2.

4.3 Experimental workflow

Depositions were done on silicon wafers with a native, about 1,6 nm thick silicon-oxide layer on top of it. The wafers are oriented in the (100) direction, scored and then broken into smaller pieces, usually about 2 x 2 cm with a diamond tip. Afterwards they are cleaned with compressed CO_2 and put in the reactor. For saturation curves experiments, usually five samples are put in the reactor. First experiments use long purge and plasma times and are usually homogenous with a variance in thickness below 10 %. Out of saturation, the deposition is very inhomogeneous. The samples then show a thickness gradient along the flow direction, decreasing from the inlet

Port number	Line
22	Heating Stage Phase 1
23	Heating Stage Phase 2
24	Plasma
25	Nitrogen
26	Nitrogen Bypass
27	Oxygen
28	Oxygen Bypass
29	Argon
30	Argon Bypass
32	ALD Valve TMA
34	ALD Valve TDMAT

Table 4.2: Arduino port setup. The oxygen lines were not used within the scope of this thesis.

towards the side were the turbomolecular pump is attached. A sketch of the reactor including wafers can be seen in 4.4.

After putting the wafers in the reactor, the line heating was turned on. For experiments at elevated temperatures the reactor mantle heating was set to 90 °C and the heating stage to 200 °C. The chamber was at first evacuated until a pressure of 100 mT was reached, then the turbomolecular pump was turned on. After reaching base pressure, which was at 14 mT with the labs relative pressure gauge, the leak reate was checked and the deposition started if it fell below 0,1 sccm. To adjust the working pressure of the system, the nitrogen flow was turned on and the turbomolecular pump partly closed to the point were a steady pressure of 100 mT was achieved. Then all lines were closed again, the plasma cable was plugged in, the plasma generator turned. The plasma matching system set to manual at a position where no reflection out of the system occured. The manual valve on the ALD bottle was opened and the chosen recipe started.

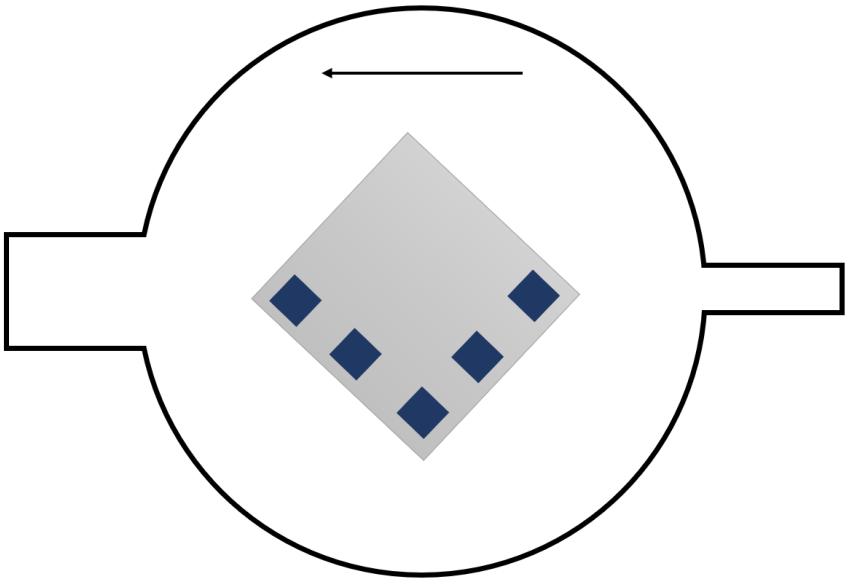

Figure 4.4: Sketch of the reactor inside. The arrow indicates the flow direction of the Argon. The turbomolecular pump is attached on the left side, the inlet for the Ar line (including the ALD precursors if pulsed) on the right side. The heating stage is shown in grey with five wafers on it. The nitrogen flows in from the top of the reactor.

4.4 Adjustable parameters

As mentioned in the first chapter , the cycle times of an ALD process are crucial to obtain self-limiting ALD growth instead of conventional CVD-like growth. It is of great importance that all four time steps lie in the saturation regime, because process parameters will influence each other as well. A very high precursor dose for example may need a longer purge time to fully remove all molecules within the reactor before the plasma process can be started.

Further process parameters are:

1. Plasma power and type
2. Operating pressure
3. Relative gas flows
4. Precursor vapor pressure – bottle temperatures
5. Reactor and line temperatures
6. Number of cycles

The reactor configuration cannot be adjusted, it is one of the unique features each custom-built reactor has and limits the ability to compare certain literature values like the purge times. Besides obvious changes in the reaction chemistry upon a change in plasma gas, the plasma power can be adjusted with a plasma generator. Usually a higher plasma power leads to hotter (higher in kinetic energy) electrons and therefore higher reactivity. Sometimes this can be compensated by longer plasma times. Since the plasma exhibited point discharges at higher powers, which influenced the homogeneity of the depositions, the plasma power was set to 60 W for depositions at elevated temperatures.

The operating pressure within the reactor - in this case altered by adjusting the manual valve towards the turbomolecular pump - changes the flow properties within the reactor and has most likely an influence on the cycle times, especially for the purging. For the sake of reproducibility, the working pressure was set to 100 mT with active 20 sccm nitrogen flow.

If now the working pressure is kept at a constant 100 mT for the nitrogen flow, but the amount of Ar which is flown into the reactor changes, the purge characteristics are different, and there therefore is variation in saturation time. For this reason, the flow ratio has been kept at 1:1 (20 sccm for both argon and nitrogen) at all times.

The amount of precursor flowing into the reactor is mainly adjusted and determined by the valve opening time. Further adjustment can be done with a change in temperature and therefore vapor pressure. This was done in the case of the TDMAT precursor, since the vapor pressure was rather low. For this reason the precursor bottle was heated up to 50 °C.

An ideal ALD process has a constant growth per cycle, independent of the number of cycles being deposited. In some real processes however, there is

an onset growth, which leads to reduced growth for the first cycle numbers. This is a surface effect and depends on the interaction between substrate and gas phase chemicals. It therefore varies with the materials processed, the substrate and its preparation. All experiments within one saturation curve have therefore been done at the same cycle number unless mentioned otherwise.

4.5 Saturation curves

In order to obtain ALD like growth instead of a conventional CVD-like process it is of great importance that the cycle times, as mentioned in chapter 1.2, are in saturation. Apriori, the saturation times are unknown and unique for each custom-built setup. A big amount of effort therefore goes into optimizing the cycle times to reduce process times and be as efficient as possible while still obtaining ALD like growth. A quick recap of how the cycle times influence the deposition is listed in the following paragraphs.

— **Precursor Dose**
  The precursor has to be pulsed long enough to completely cover the substrate within the whole reactor and achieve saturation in the growth regime. If the pulse time is too low, the deposition lacks homogeinity, the GPC is reduced and the thin film itself is getting less dense due to higher porosity caused by vacancies.
— **Plasma dose**
  The plasma exposure must be long enough for all the free radicals to interact with the surface atoms and grow on the substrate. If the plasma exposure is chosen to be short or not turned on at all, the growth and film density is reduced.
— **Purge times**
  The purge times for both after the plasma and the precursor need to be long enough to divide the two interacting processes of the deposition in order to avoid gas phase reactions (which then would result in classical CVD growth). In ALD only reactions on the substrate surface should occur.

In the following chapters the experiments to optimize the saturation times are explained in chronological order. A comprehensible insight on how the optimized recipe for depositions with TMA precursor and nitrogen plasma was found is given. It is also explained, why some changes to the system or process were necessary. At first depositions of aluminum nitride were started, since this precursor was available already and both processes needed to be optimized separately. Issues with the low vapor pressure of the TDMAT precursor followed by a clogging of the lines and the precursor bottle itself due to internal reactions after the lockdown made it impossible to do further testing on TDMAT within the scope of this thesis.

4.6 Deposition at room temperature for aluminum nitride

Since no literature was available about room temperature depositions and prior experiments on ZnO on this reactor have shown good results in terms of chemical composition, depositions on room temperature were performed. Starting times were initially chosen to be 15 s for each of the process times excluding the precursor pulse. For later experiments, only elevated temperatures where used, results obtained at room temperature were used as a guide for saturation times at elevated temperatures. The plasma power was initially set to 100 W and then reduced later in the process. As mentioned in the following chapter, the plasma became more and more inhomogeneous, with some point discharges at the top electrode grid and the power therefore had to be reduced.

4.6.1 TMA saturation at room temperature

Contrary to later results this deposition was done just before the reactor was revamped due to line clogging where the layout was changed. After initial deposition at a working pressure of 60 mT, the plasma became less and less stable at both 20 and 100 W and the working pressure with active

nitrogen flow was increased to 100 mT. The deposition parameters can be seen in 4.3.

TMA Dose /ms	TMA purge /s	Plasma dose /s	Plasma purge /s
20	15	15	15
30	15	15	15
50	15	15	15
100	15	15	15
200	15	15	15

Table 4.3: TMA saturation time experiments at room temperature

4.6.2 Purge after precursor saturation at room temperature

After successful determination of the precursor pulse time, which was found to be at 50 ms, the purge time after the TMA pulse was optimized. After two runs at 30 and 22 s purge time, one of the lines was clogged and the reactor lines were rebuilt. The layout of the system was changed and depositions were repeated. All depositions which are listed 4.4 were done after the reconstruction.

TMA Dose /ms	TMA purge /s	Plasma dose /s	Plasma purge /s
50	15	30	15
50	15	22	15
50	15	15	15
50	15	8	15

Table 4.4: Purge after precursor saturation time experiments at room temperature

4.6.3 Plasma purge saturation at room temperature

The purge time after the precursor pulse was found to be at 22 s and therefore above the time in which the precursor pulse was initially tested. The optimum pulse time (which might be influenced by the purge time) was kept at 50 ms initially and planned to be retested later on with a more

optimized process. In the next step the purge time after the plasma process was optimized. The timesteps used in this series can be seen in 4.5.

TMA Dose /ms	TMA purge /s	Plasma dose /s	Plasma purge /s
50	22	15	30
50	22	15	22
50	22	15	15
50	22	15	8

Table 4.5: Purge after plasma saturation time experiments at room temperature

4.6.4 Plasma saturation at room temperature

After determining the optimum purge time for the plasma, which was found to be at 15 s, the plasma time was left to be determined. However, issues with the plasma became apparent, showing some point discharges on the top electrode grid which could be seen through the window as a glowing point on the top. While it did not show up on every cycle when the plasma was fired, the frequency of it increased- Wafers located close to the discharge points locations showed higher film growth, homogeneity was not obtained anymore.

To overcome this problem, many different approaches have been taken. This includes the change of the working pressure within the system, depositions with a mixed plasma of argon and nitrogen (both at 10 sccm flow), remounting and swapping out the top electrode grid and changing the plasma cable. The only way to consistently solve this issue was to reduce the plasma power to 20 W. As mentioned in the first chapter and in 4.4, a reduced plasma power leads to a reduction in temperature of the radicals, increasing the saturation time. The growth per cycle was still very high at about 0,6 nm per cycle and therefore above the unit cell size of AlN.

With the change of the plasma power, all cycle times have been increased again in order to eliminate the possibility of low purge times interfering with the film growth and therefore have been chosen to be set at 60 s.

The plasma time was set to 100 s and gradually decreased. This was done, since it was shown with other nitrogen plasma deposition, for example with trimethyl-indium, that high plasma up to 100 s times are necassry in order to stay in saturation. In this case, the GPC does decrease with lower plasma times, but increased if the plasma is pulsed shorter. This may occur due to the fact that not all organic compounds - most likely carbon hydrides - can be cleaned from the surface and are occupying the active surface sites. Once the plasma is used long enough, the carbons or carbon-hydrides are removed and nitrogen atoms can bond on the active Indium sites. [41]

TMA Dose /ms	TMA purge /s	Plasma dose /s	Plasma purge /s
50	60	100	60
50	60	50	60
50	60	25	60
50	60	12	60

Table 4.6: Plasma saturation time experiments at room temperature

The decrease in plasma power led to a rather high plasma saturation time of 25 s, the growth per cycle however was still above reported literature values, where different types of plasma were used.

4.7 Deposition at elevated temperature for aluminum nitride

After optimization of the four process times still did not show any significant reduction of the growth per cycle, XRR measurements indicated a low mass density and the ellipsometry measurements showed a low refractive index, it was suspected that a high amount of organic groups is deposited in the film. In order to prevent organic residues, the heating stage of the reactor was repaired, and 200 °C as deposition temperature used. The wall heating was set to 90 °C and the line heating to 40 °C.

A change in temperature has major influence on the reaction kinetics and therefore again, the saturation times have been optimized. The purge times

were set to 60 s, the plasma time to 100 s and precursor time was doubled, and later readjusted since the temperature should have less influence and additional waste of the precursor is to be avoided. The plasma power was now set to 20 W and 60 cycles have been deposited in each process.

4.7.1 Plasma saturation at elevated temperature

Since the plasma cycle time was the longest, it was optimized at first, with a starting time of 100 s. Depositions done within this series are shown in 4.7. For all depositions a nitrogen flow of at least 8 s was necessary in order to obtain the operating pressure, in which the plasma was stable. As can be seen in the table, a thermal ALD deposition also has been done, the plasma was not ignited, a nitrogen flow was introduced for 8 s in the chamber.

TMA Dose /ms	TMA purge /s	Plasma dose /s	Plasma purge /s
100	60	100	60
100	60	50	60
100	60	25	60
100	60	15	60
100	60	8	60
100	60	4	60
100	60	2	60
100	60	0	60

Table 4.7: Plasma saturation time experiments

4.7.2 Plasma purge saturation at elevated temperature

While ellipsometry measurements showed sufficient plasma at 2 s already, during some depositions the plasma did not fire immediately, a plasma time of 4 s was chosen. After this, the plasma purge saturation time was investigated. The cycle times in use can be seen in table 4.8.

TMA Dose /ms	TMA purge /s	Plasma dose /s	Plasma purge /s
100	60	4	60
100	60	4	30
100	60	4	15
100	60	4	8
100	60	4	4

Table 4.8: Plasma purge saturation time experiments

4.7.3 Precursor saturation at elevated temperature

A purge time of 8 s was found to be still in saturation and therefore used for further processes. In the next step the precursor time was adjusted in order to find the optimum pulse time. The parameters are shown in table 4.9.

TMA Dose /ms	TMA purge /s	Plasma dose /s	Plasma purge /s
100	60	4	8
50	60	4	8
25	60	4	8

Table 4.9: Precursor saturation time experiments

4.7.4 Precursor purge saturation at elevated temperature

Similar to depositions at room temperature, a pulse time for the aluminum precursor of 50 ms was found to be sufficient and was therefore used to minimize the purge time after the precursor pulse. Once again, depositions were started at 60 s of purge time and reduced until saturation was not achieved anymore. The cycle times used can be seen in table 4.10.

TMA Dose /ms	TMA purge /s	Plasma dose /s	Plasma purge /s
50	60	4	8
50	30	4	8
50	15	4	8
50	8	4	8

Table 4.10: Purge after precursor saturation time experiments

4.7.5 Optimum recipe and thicker samples

After finishing the last optimization step, the optimum recipe at 200 °C and 20 W plasma at a working pressure of 100 mT (with active nitrogen flow) was found. It is listed in 4.11.

TMA Dose /ms	TMA purge /s	Plasma dose /s	Plasma purge /s
50	15	4	8

Table 4.11: Optimum recipe at 200 °C

With this recipe thicker samples have been created, in order to allow for better analysis of these samples. Depositions of 480 and 560 cycles were done. A high film thickness is often required or beneficial, such as XRD measurements to determine the crystallinity.

4.8 Deposition of titanium nitride

First runs of depositions with titanium nitride were done after the aluminum nitride recipe was finished and therefore the conditions were already adjusted. As mentioned in 4.1.1 a heat bath was built and installed to increase the vapor pressure of the precursor. The oil was heated up to a temperature of 50 °C.

Initially, tests were done to check the pressure increase of the system after the precursor was opened. While first depositions were done with long cycle

times and a precursor time of up to 5 s, low growth and uneven thickness distribution were measured, with a very low GPC (about 10% compared to reported literature values) at the inlet of the reactor and no sign of any growth on the other side.

Further testing has then been done with a reduced operating pressure of 50 mT of the vacuum chamber as well as with an increased plasma power of 60 W. Testing has also been done with multiple pulses in a single cycle with varying durations, however the growth was still very limited and inhomgenous. Furthermore, already existing AlN films were used as substrates to exclude the choice of substrate as a deciding factor. No significant deposition in terms of thickness (XRR) and chemical composition via x-ray fluorescence was achieved.

After this the installation of a bubbler line was planned, however the lab was not accessible due to the 2020 covid-19 pandemic and the labs shutdown for about eight weeks starting with mid of March. In this time the pumps were shut down and the reactor was not in use.

After the shutdown of the lab the bubbler line was installed, it was used to bubble argon into the precursor bottle and increase the flow. A new line was laid from the mass flow controller to the inlet directly. Instead of a single line next to the bypass, a second line flowing towards the precursor bottle was mounted. Equal to the outlet of the precursor bottle, the inlet was controlled with an ALD valve to precisely control the argon flow towards the precursor.

After this installation further tests were done and still no deposition was obtained. The pressure built up in the bottle instead of being released through the ALD valve, indicating a congestion between the valve of precursor and the reactor. The shared line towards the reactor was confirmed to be not congested. This pointed to the issue that the precursor bottle itself is clogged. After consulting with engineers from Dockweiler Chemicals, the manufacturer of the precursor bottle, who told us that TDMAT is very reactive with oxygen (and therefore air as well) and produces powdery titanium oxides, it was expected that oxidation occurred during the downtime.

The issue most likely stems from a very minor leak between the ALD valve and the reactor. During the shutdown, enough time passed, for incoming air

to flow in and then react once the bottle was opened again. This requires the replacement of the bottle, since the bottle itself is clogged. This however was not possible without going beyond the already extended timeframe of this thesis due to long delivery times of the precursor. No further depositions have been done and deposition of TiN was unfortunately not succesful.

5 Saturation regime determination

Saturation curves of aluminum nitride for both depositions at room temperature and 200 °C are presented in this part. In this analysis the growth per cycle is drawn over various cycle times. The error bars in the measurements result from the standard deviation of the thickness of the five wafers analyzed each deposition. Values marked in red indicate that this deposition time is the lowest time still to be in saturation and has been used in further processes.

The thickness measurements were conducted with spectroscopic ellipsometry. Since SE is not a direct method, a Cauchy model was used to determine the thickness and optical constants (see 2.1). Unless stated otherwise, a single optical model was used for all wafers in saturation for better comparability. In saturation, the deviations between each depositions model are rather small. For depositions out of saturation deposition a new model was created.

The obtained thickness values were divided by the number of cycles to obtain the GPC. A chronological record of the depositions and changes to the reactor and the procedure to optimize the process times was explained in the latter chapter.

5.1 Saturation regime of aluminum nitride at room remperature

In this section the saturation curves of aluminum nitride at room temperature are presented.

5.1.1 Precursor saturation at room temperature

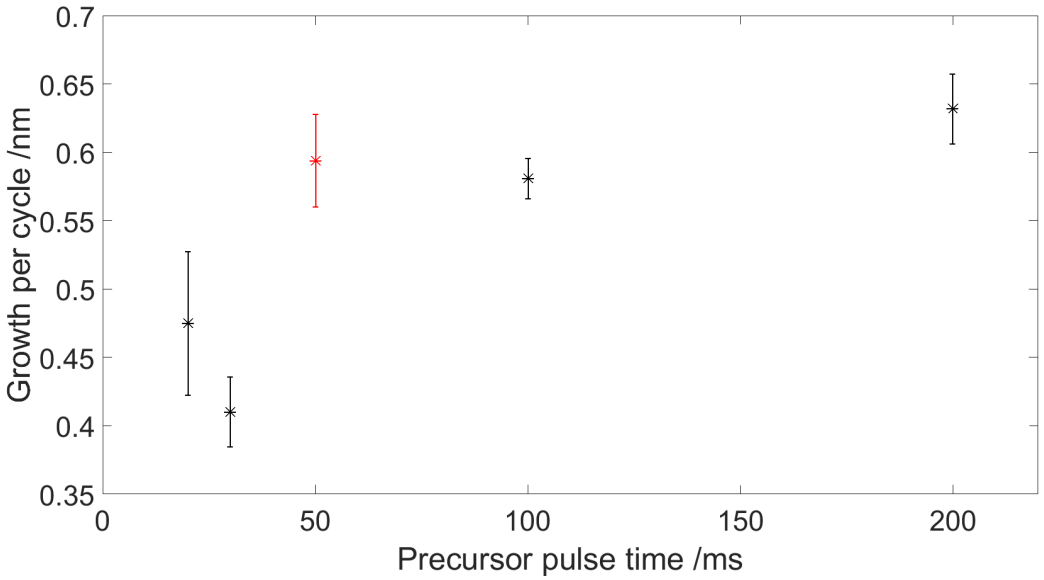

Figure 5.1: Precursor saturation curve at room temperature at 100 cycles.

The change in growth per cycle depending on the precursor dose can be seen in figure 5.1. The precursor (TMA) dose shows a rather signifcant drop off below 50 ms and a plateau above that. For precursor times of 50 ms the process is fully saturated and self-limiting ALD growth can be achieved. The growth itself however, is rather high at 0,6 nm/cycle. This deposition was done before the reconstruction and at a reduced working pressure of 60 mT. At only 20 ms precursor time, the standard deviation increased due to a gradual decrease of thickness for wafers further away from the inlet.

This is also another indicator that the process is not in the saturation and full coverage is not achieved anymore.

A precursor pulse time of 50 ms led to a GPC of 0,59 nm/cycle.

The reactor was remodeled and due to plasma stability issues the working pressure was increased to 100 mT. Two further depositions were conducted at 50 and 100 ms to ensure saturation of the precursor. At 50 ms, the GPC was measured to be at 0,66 nm per cycle and 0,58 at 100 ms, confirming that saturation was still achieved.

5.1.2 Precursor purge saturation at room temperature

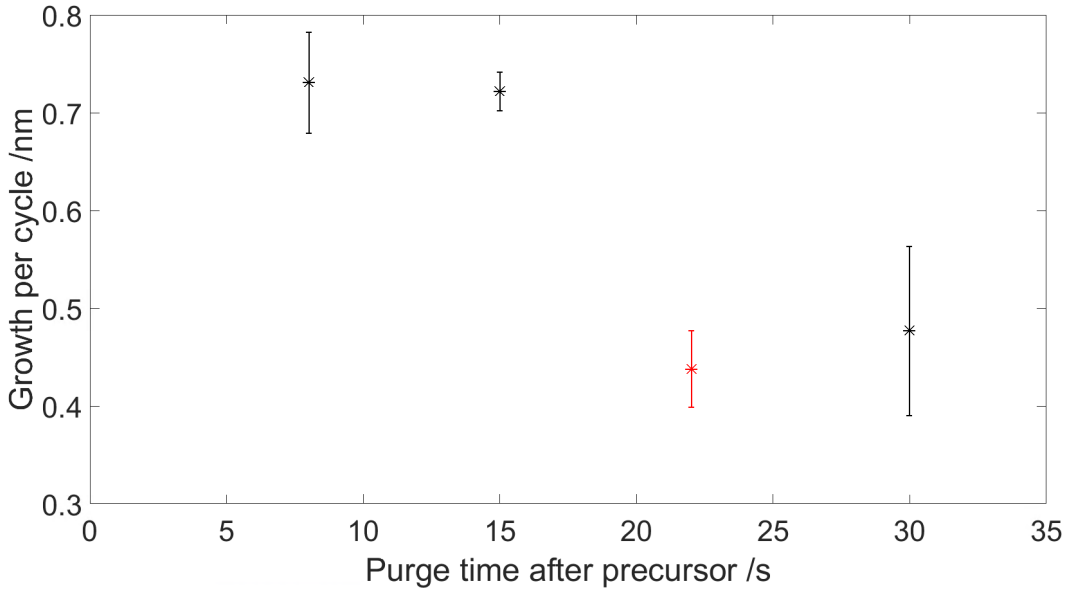

Figure 5.2: Precursor purge saturation curve at room temperature at 40 cycles.

The saturation curve for the purge time after the precursor can be seen in figure 5.2. A significant increase of 70 % in GPC can be seen for purge times of 15 s and lower, and therefore the purge time was chosen to be 22 s. If the purge time is too low, not all the remaining precursor molecules in the reaction chamber can be flushed out when the plasma is ignited, leading to gas phase reactions and therefore increased CVD-like growth.

A purge time of 22 s led to a GPC of 0,44 nm/cyle.

5.1.3 Plasma purge saturation at room temperature

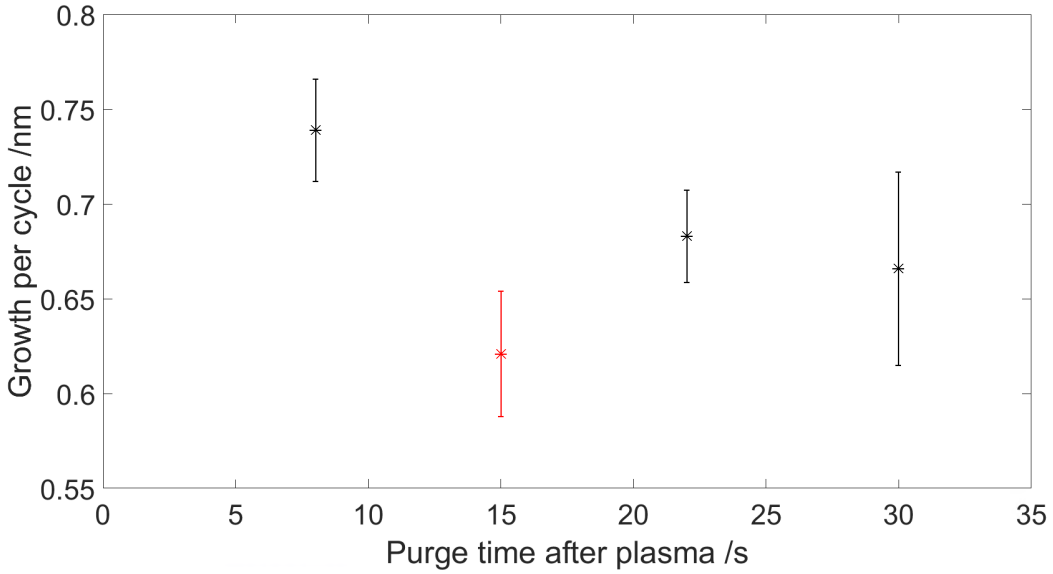

Figure 5.3: Plasma purge saturation curve at room temperature at 60 cycles.

In figure 5.3 the dependence of the plasma purge time on the growth per cycle can be seen. Similar to the purge time after the precursor, it can come to reactions in the gas phase, and increase the GPC which is to be avoided. For a purge time below 15 s the process was not in saturation anymore.

A purge time of 15 s led to a GPC of 0,62 nm/cycle.

5.1.4 Plasma saturation at room temperature

The plasma saturation curve is shown in 5.4. As point discharges with the plasma appeared when firing, the plasma power was reduced to 20 W and process times were set to 60 s for the purge process. A plasma time of 25 s was found to be sufficient. A reduction to the plasma time decreased the

film growth, the plasma has not enough time to activate the sites of the Al on the surface and the growth is reduced. The growth in saturation was still significant above literature, in which depositions at elevated temperatures were conducted and the film density was very low as well. This can hint to both organic impurities and/or porous films.

A plasma time of 22 led to a GPC of 0,60 nm/cycle.

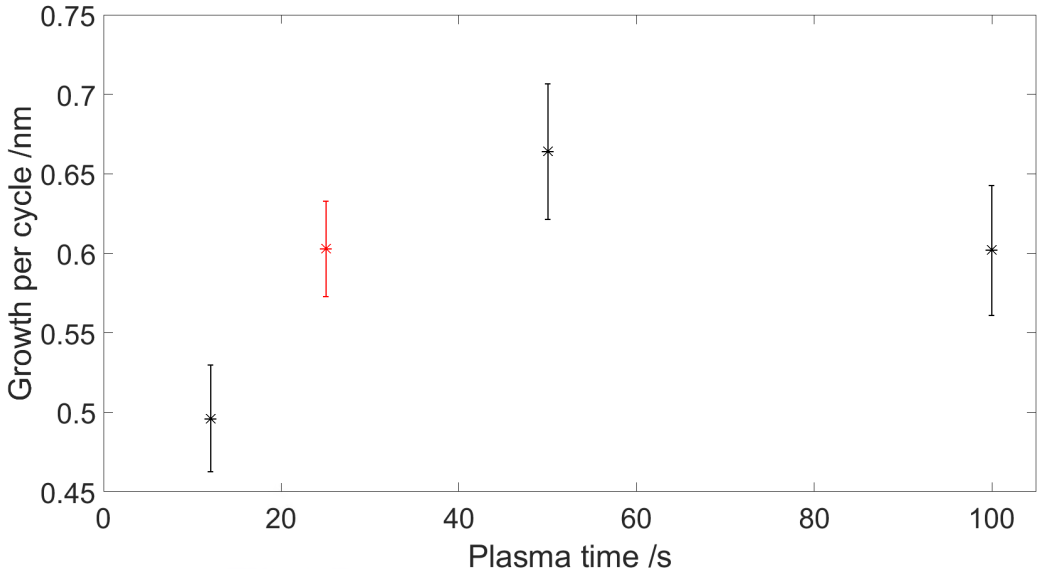

Figure 5.4: Plasma saturation curve at room temperature at 60 cycles.

5.2 Saturation regime of aluminum nitride at elevated temperature

After no reduction of the film growth per cycle could be achieved, depositions were conducted at 200 °C and 20 W plasma power. All depositions were done at a working pressure of 100 mT and 60 cycles. As described in 5.4 in further detail, the purge times were increased to get an extensive understanding of the process.

5.2.1 Plasma saturation at elevated temperature

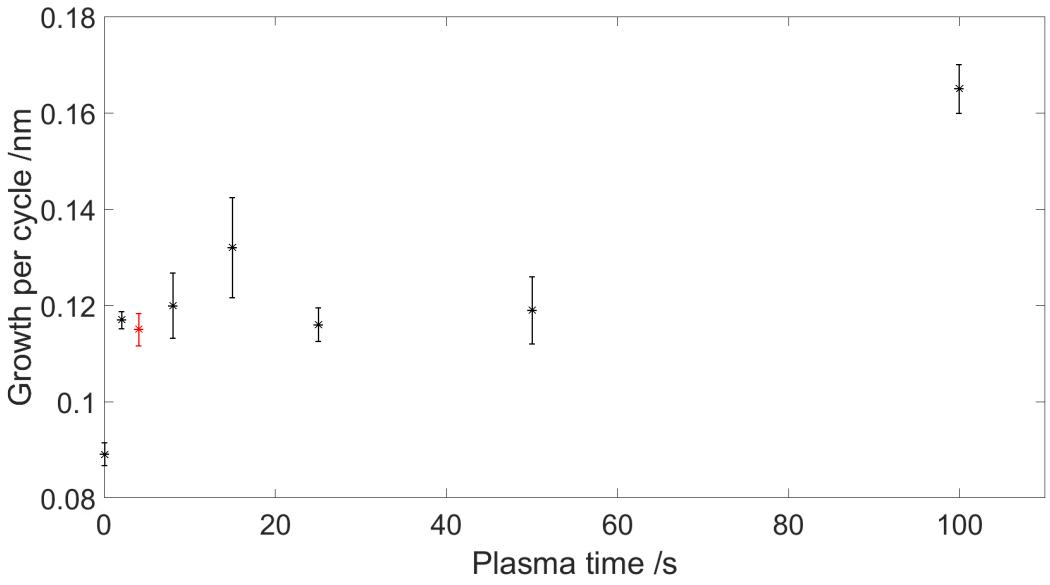

Figure 5.5: Plasma saturation curve at 200 °C

At first the plasma time was optimized, since it had the longest cycle time by default. The results can be seen in 5.5. One can see a very broad saturation regime between 2 and 50 s, in which the deposition is constant within the statistical deviation.

For extended plasma times the growth is once again increasing. A long plasma exposure time can cause additional reactions on the surface, and open up active sites, which allows for further secondary reactions therefore and therefore leads to increased growth. The film thickness was increased while the refractive index was reduced from 1,87 to 1,82, which indicates a higher thin film porosity.

On the lower end a short exposure of only two seconds was enough to enhance the growth during the process. A thermal ALD process was also conducted. The growth was reduced from about 0,12 nm/cycle to 0,09 nm/cycle. Furthermore the refractive index was higher at 1,92, compared to 1,82 for the plasma ALD process, indicating a change in thin film composition.

Some cycles showed a delay in plasma ignition of 1-2 s and therefore 4 s plasma time was chosen for further depositions. A GPC of 0,11 nm/cycle was achieved.

5.2.2 Plasma purge saturation at elevated temperature

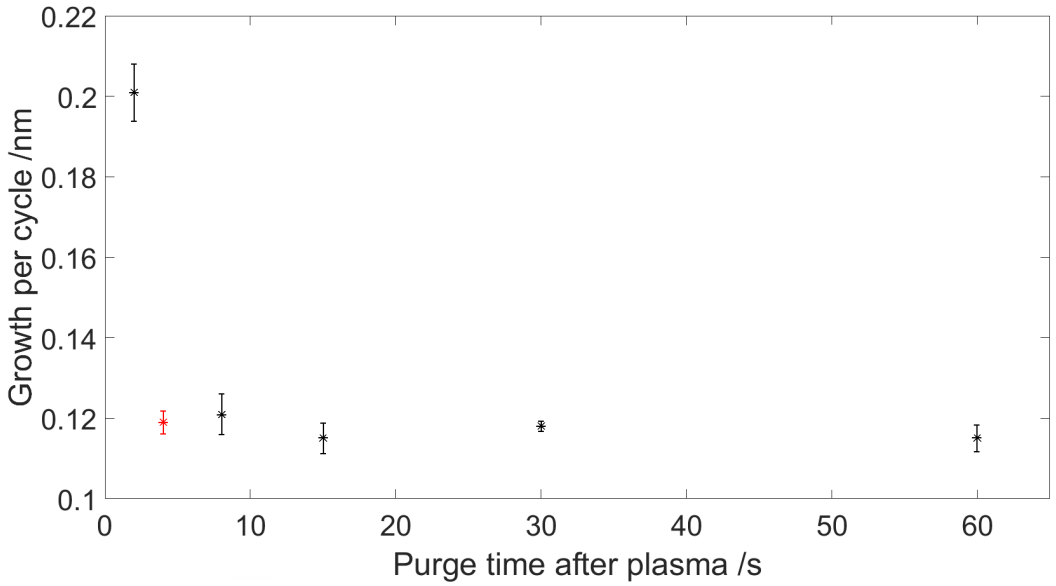

Figure 5.6: Plasma purge saturation curve at 200 °C

The saturation graph for the plasma purge can be seen in 5.6. The cut-off is rather significant here, with no major difference in growth per cycle between 60 and 4 s at all. If the purge time is reduced to 2 s however, the GPC almost doubles, since there are still reactive plasma radicals in the chamber when the precursor is pulsed in. As explained before, this leads to gas phase reactions, the growth is not limited by its cycles but time limited and therefore the process is not in the ALD regime anymore.

A plasma purge time of 4 s led to a growth of 0,12 nm/cycle.

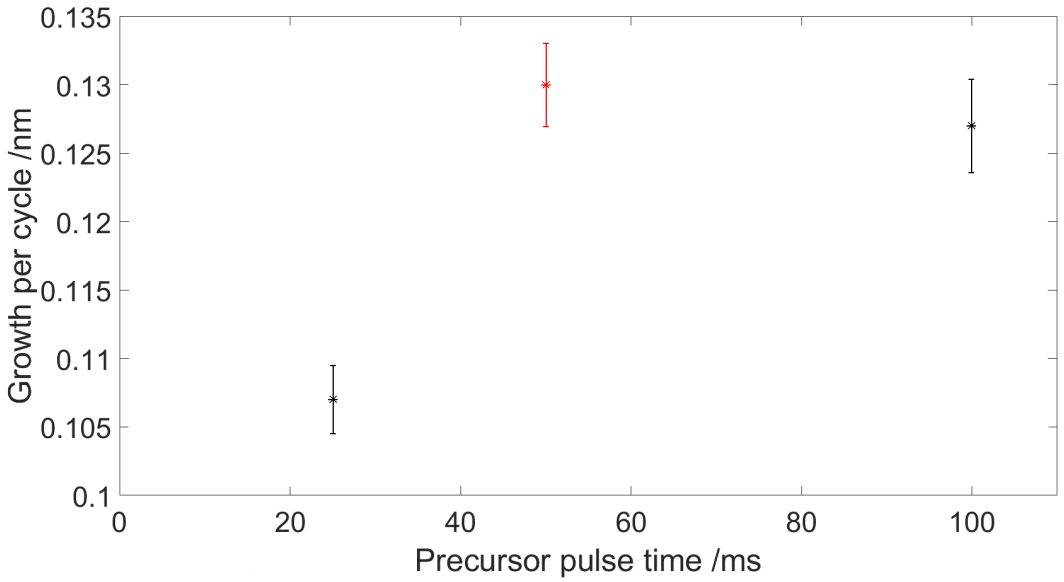

Figure 5.7: Precursor saturation curve at 200 °C

5.2.3 Precursor saturation at elevated temperatue

The precursor saturation was once again tested and the saturation time was found to be unchanged at 50 ms compared to room temperature depositions. Therefore the same amount of precursor is required to achieve full coverage of the surface. The growthrate however, is only about a fifth of the initial deposition with the same precursor pulse time. This indicates that at room temperature a lot of impurities and organic compounds grow on the surface as well. The results can be seen in figure 5.7.

At a precursor pulse time of 50 ms a GPC 0,13 nm/cycle was achieved.

5.2.4 Precursor saturation at elevated temperature

The final step to be optimized was the saturation time after the precursor pulse. The related graph can be seen in figure 5.8. Similar to the plasma purge graph and according to theory, a rather significant increase in GPC can be seen once the process is not in saturation anymore. This occurs for

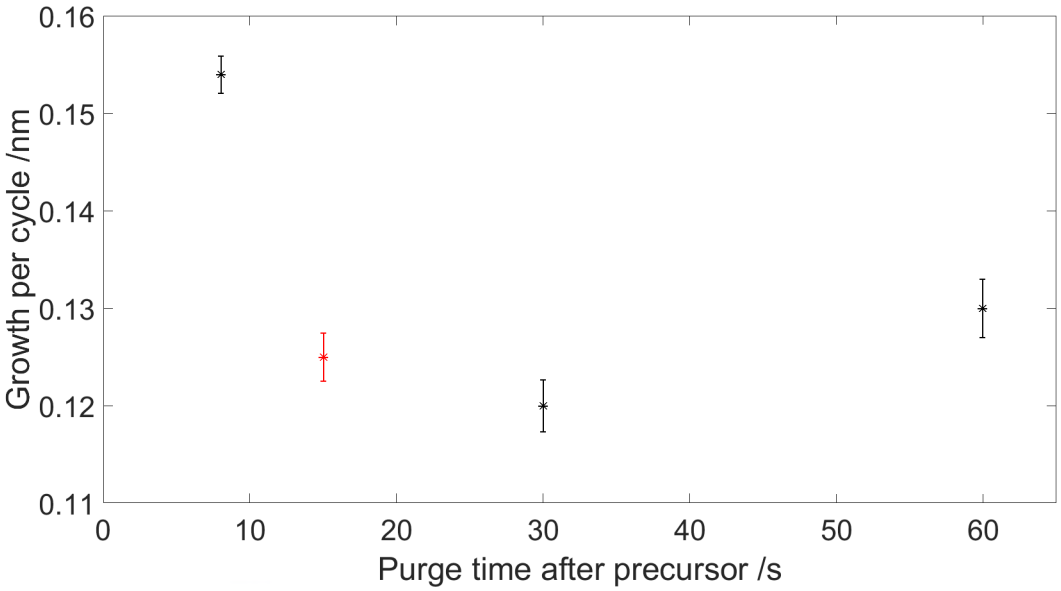

Figure 5.8: Precursor purge saturation curve at 200 °C

purge times below 15 s, where the GPC increases up to 0,15 nm/cycle at 8 s.

At a precursor purge time of 15 s a GPC of 0,13 nm/cycle was achieved.

The recipe was optimized, thicker thin films were produced and analyzed.

6 Thin film analysis

This chapter is dedicated to the analysis of thin films deposited with nitrogen plasma and TDMAT precursor. Films prepared at room temperature and at 200 °C were studied. XRD data is used to determine the crystallinity, XRR is used to characterize the thickness and the density of the thin films. FTIR allows the analysis of stretching and bending of intermolecular bonds. An introduction to these methods can be found in chapter 3.

6.1 Thin film characterization of room temperature depositions

Films deposited at room temperature were analyzed with spectroscopic ellipsometry. As described in 4.6.4, times of t=(25/60/0.05/60) s were used for 60 cycles, which led to a GPC of 0,60 nm/cycle on average. The optical properties of the five coated wafers are very similar to each other,and the models fitted do not differ significantly from each other.

A study conducted by Van Bui et al. [42] analyzed the refractive index of ALD deposited AlN thin films. Especially for thermal ALD it was shown that the refractive index is increasing with the thickness up until about 50 nm for thermal ALD. This effect was also apparent for PEALD done with ammonia and nitrogen-hydrogen mixed plasma, however not as distinct. The refractive index for both plasma types was 1,85 at 35 nm thickness.

The obtained model for the refractive index can be seen in figure 6.1. Additionally to the experimental data, an optical model by Khoshman and Kordesch [43] was added. In this study 50 nm thick reactive-sputtered amorphous AlN films were produced and analyzed with spectroscopic

ellipsometry. The extinction coefficient of the refractive index was left out due to the high uncertainty, being in the same range as the value itself and therefore not allowing for a physical meaningful statement. The refractive index at 632,8 nm was 1,60 for a 35 nm thick film.

The low refractive index in combination with a high growth rate, larger than the unit cell size, indicates the existence of organic impurities. These stem from the precursor, were three remaining methyl groups are left over upon reactions with the surface, were the aluminium atom is adsorbed. It therefore was expected that the residues are mainly carbon and hydrogen bonds that additionally grow on the film, lowering the film quality.

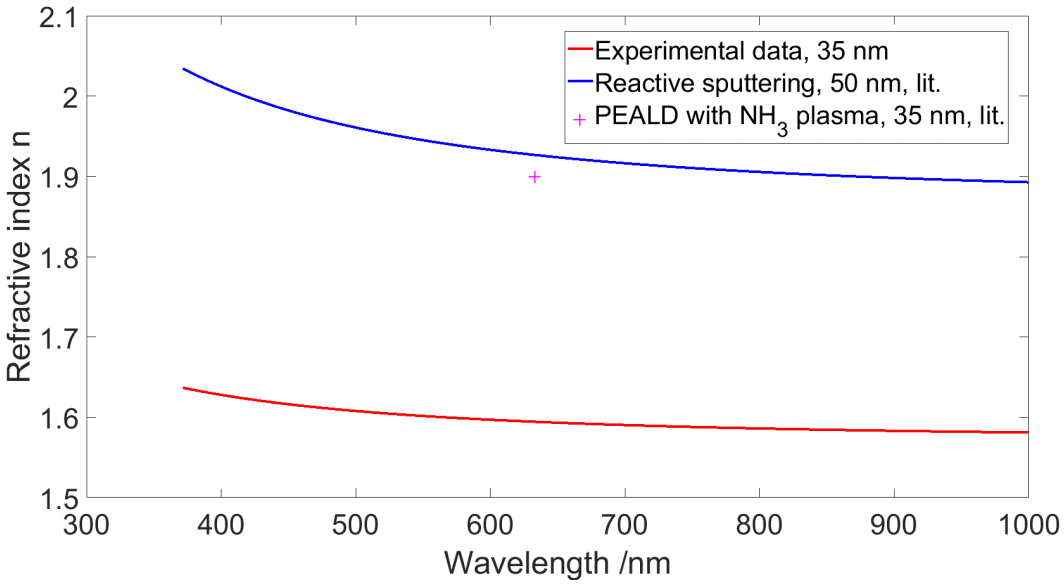

Figure 6.1: Refractive index of AlN. Experimental data obtained with SE in red, optical model for reactive-sputtered films in blue [43] and obtained by plasma ALD with ammonia plasma in pink [42]

6.2 Thin film characterization of films deposited at elevated temperature

6.2.1 Spectroscopic ellipsometry of films deposited at elevated temperature

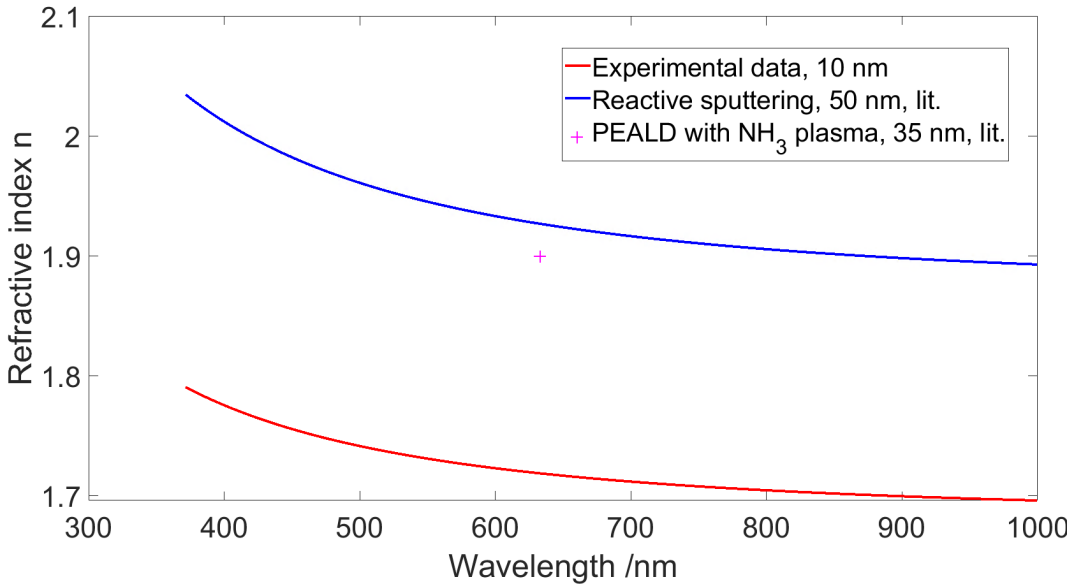

Figure 6.2: Refractive index of AlN. Experimental data obtained with SE in red, optical model for reactive sputtered films in blue [43] and obtained by plasma ALD with ammonia plasma in pink [42]

At elevated temperature, the film growth was reduced by a factor of five and the refractive index was increasing as well. As can be seen in figure 6.2 the optical model is still not lining up with literature values. The optical model for thin wafers with a thickness of 80 cycles (which resulted to a film thickness of about 10 nm) lined up with the optical models obtained for thicker wafers. This is of importance because the significance of the model for thicker samples is higher, leading to an increased error for small deviations compared to thinner samples. For thicker samples, the growth per cycle for longer depositions was increased from 0,11 to 0,15 nm/cycle

and therefore about 50- 60 % above literature, were NH_3 and N_2-H_2 mixed plasma was used. (see 2.1.3).

6.2.2 X-ray-diffraction analysis

X-ray diffraction measurements were performed for samples deposited at 200 °C. A scan over the whole range has been conducted in order to get an overview of the sample. The initial deposition consisting of 560 cycles was done in the beginning of March, with the XRD deposition done the day after. The result can be seen in figure 6.3.

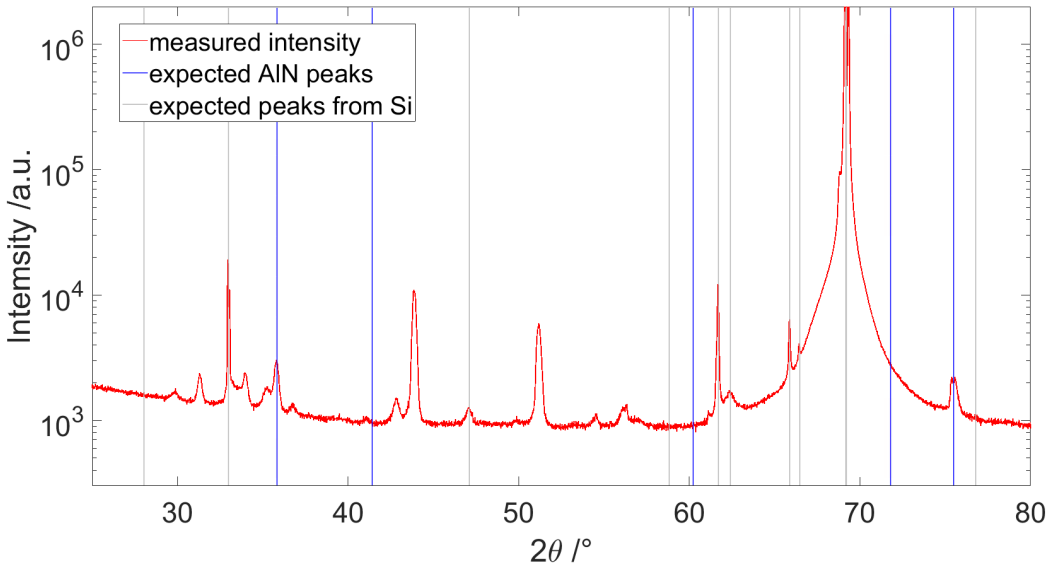

Figure 6.3: X-ray diffraction scan of deposited AlN at 200 °C and 560 cycles. According to ellipsometry, the wafer had a thickness of 89 nm. The measured intensity can be seen in red. Expected AlN peaks are marked in blue, grey lines indicate that do not directly relate to the thin film

The expected peaks of AlN are marked in blue. Two peaks at 35,8 ° and 75,5 ° show crystallinity and are lining up with the theoretical diffraction pattern. The first one arises from the (002) peak of AlN and the second from the (222) peak. Peaks marked in grey do not directly stem from the sample but the surrounding itself. The main big peak below 70 ° is the (100) peak

from the silicon substrate for the k_α-radiation. The peaks at 61,7 and 62,2 ° stem from the copper source as well, from the slightly higher energetic k_β-radiation. The peak at 33 ° matches the spacing of the (200) peak of the silicon substrate.

In between the k_α and k_β-peak at 65,9 °, a rather sharp peak can be allocated to the wavelength of wolfram k_α-radiation. Wolfram is used as kathode in order to produce X-ray radiation and can dissolve in small amounts from the tube. Other grey vertical lines are expected peaks from the wafer processing. The wafers were scored with a diamond tip and then broken, which creates small crystalline silicon dust particles that can remain on the wafer even after cleaning them with compressed CO_2. A peak at 47 ° was be observed.

The HighScore software by Panalytical has been used, were it is possible to mark peaks (or do an automatic search) and then use the match-and-search function, which has a database of existing patterns and tries to find a possible fit for the peaks. It was not possible however to match a suiting pre-existing pattern to the experimentally gained data and the remaining peaks could not be identified.

In order to improve the crystallinity, annealing measurements were planned to be performed. The annealing is done on the stage of the XRD device and therefore allows for in-situ measurement. The samples can be heated up to 1100 °C under inert nitrogen atmosphere to prevent oxidation at high temperatures. Due to the shutdown of the laboratory caused by the covid-19 pandemic, the annealing experiments were postponed and had to be conducted afterwards.

A published study showed annealed amorphous AlN samples under N_2 atmosphere deposited with PEALD on GaN exhibit increased crystallinity of hexagonal AlN structure at 800 °C and 1000 °C, whereas at 500 °C and below, no crystalline formation could be observed. Cao et al. [44] conducted XPS experiments and showed that at 800 °C and above, N-O-Al bonds were broken and Al-N bonds formed instead. This causes a decrease in resistance and leads to semiconductor-like conductive behavior. [44].

The sample was remeasured before the heating stage was used. The XRD profile completely changed over time however und it was suspected that

the sample aged in the meantime. This was confirmed by ellipsometry measurements, in which an increase in film thickness was measured in addition to the change of color of the samples. The batch of samples grew from 90 nm to about 130-140 nm, while the refractive index went down from 1,71 to 1,57.

Fresh samples were produced twice and analyzed the day after, however it was not possible to replicate the results shown in figure 6.3. The XRD pattern of the newly produced samples align with spectra taken from the aged samples, which was taken after the shutdown of the laboratory. Measurements were performed at room temperature, 200, 500, 800, 850 and 1100 °C, respectively. The heating rate was set to 20 °C/min. The graph can be seen in figure 6.4.

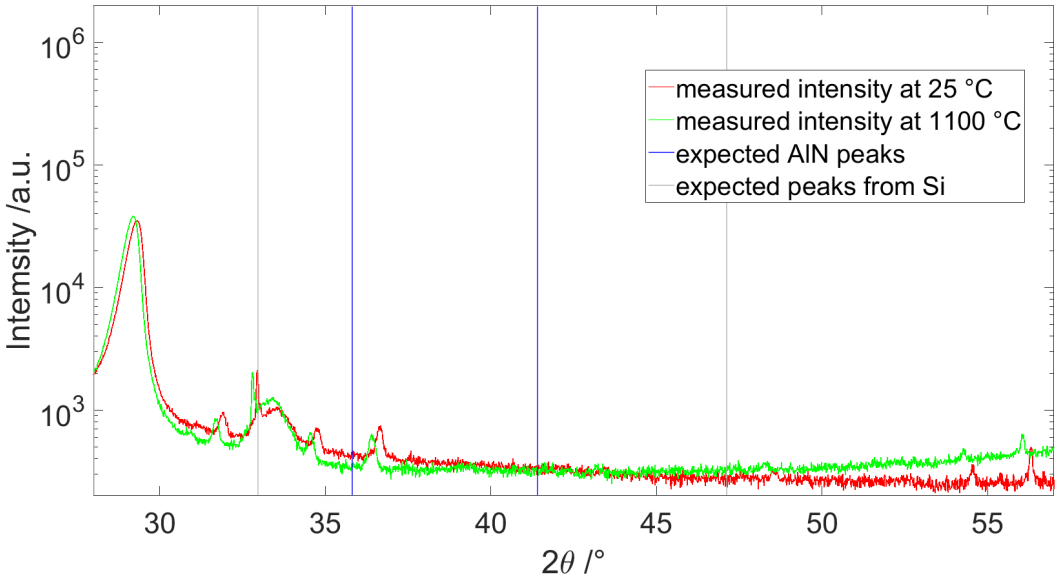

Figure 6.4: X-ray diffraction scan of deposited AlN at 200 °C and 480 cycles. The sample was heated up gradually to 1100 °C and analyzed in situ

The annealing of the deposited films showed no increase in crystallinity at any incident angle. The gradual shift to the left with increasing temperature of the whole spectrum is caused by the thermal expansion of the thin film due to heating, slightly increasing the lattice constants and therefore decreasing the angle at which Bragg's Law is fulfilled.

The very broad peak between 27 and 30 °C comes from the graphite dome that was in use to contain the nitrogen atmosphere. The dome reduced the total intensity to about the half of its origin, which required an increased data acquisition time.

6.2.3 X-ray-reflectivity analysis

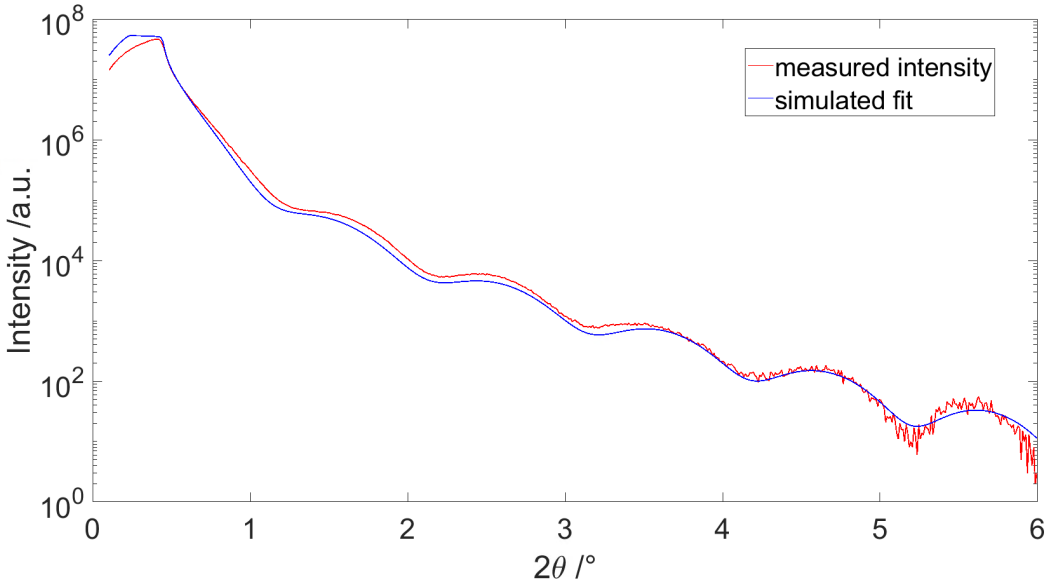

Figure 6.5: X-ray reflecivity measurement of a saturated deposition with 80 cycles. The measured intensity can be seen in red, the simulated fit in blue.

X-ray reflectivity measurements also have been conducted to verify the obtained results from the ellipsometry measurements, since it is not a direct method and error prone if the wrong model is chosen. The thickness can be obtained from the frequency of the fringes, as can be seen in figure 6.5. It was determined to be 9,4 nm and a roughness 0,4 nm was measured. This means that the deposition consists of a single homogenous monolayer and the surface is rather smooth. The density in this fit was found to be 3,58 g/cm^3, which is above the literature value of 3,26 g/cm^3 for bulk AlN. [45]

Thickness analysis of the same sample with spectroscopic ellipsometry showed a minimum error at a thickness of 10,7 nm, however the error estimation was very similar between a simulated thickness of 9 and 11 nm and therefore lines up with the obtained results from the XRR measurements.

X-ray analysis of a deposition done with 560 cycles has also been conducted. The high film thickness, in theory, leads to a high frequency of the Kissing fringes in the XRR spectra. The reflectivity pattern can be seen in figure 6.6. This measurement was conducted after the lockdown.

Contrary to thinner samples, the Kissing fringes oscillate at a higher frequency, however in this measurement, they are not very distinct. This indicates that the thin film is not fully homogenous and consists of multiple layers with a slight change in refractive index. According to the Fresnel equations, reflectance occurs upon a change in refractive index, which then leads to multiple reflections within the system and smears out the Kissing fringes. The simulation assumes a homogenous monolayer, in which the fringes are very distinct, as described in the last chapter.

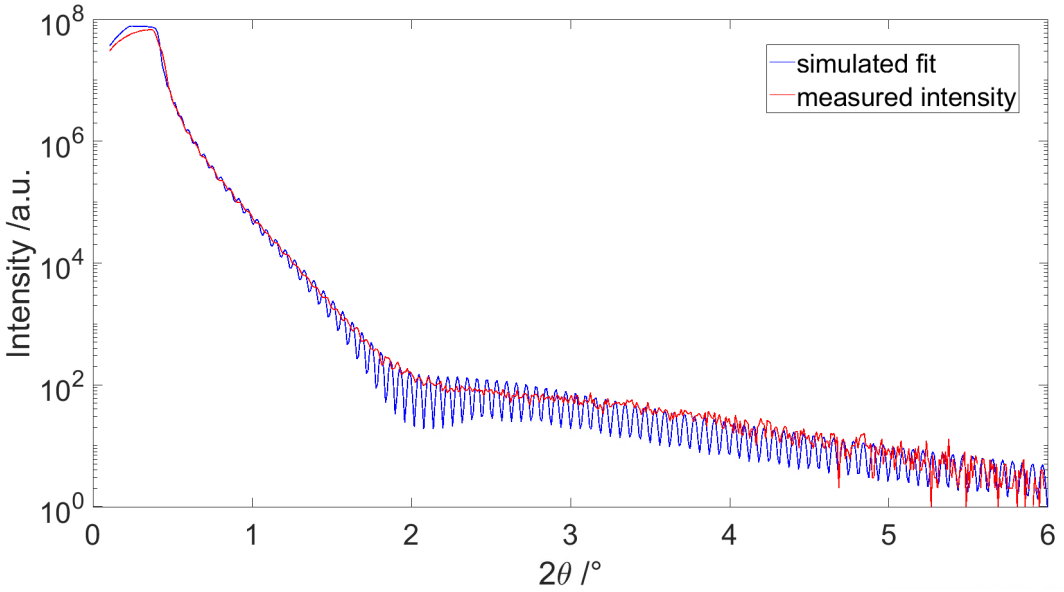

Figure 6.6: X-ray reflectivity measurement of a saturated deposition with 560 cycles. The measured intensity can be seen in red, the simulated fit in blue.

The angle of total internal reflection was significantly lower - maximum intensity was reached at 0,375 ° compared to 0,415 °, which means that the electron density in the film is lower as well. Fitting with aluminum nitride estimates a film density of 2,0 g/cm^3, which is not only below the initial measured density but also well below the estimated literature value.

The low film density in combination with the exhibited multilayer behavior leads to the assumption that the film exhibits some porosity. While the film itself got thicker, not only the mass density was reduced to well below the bulk value of AlN, also the refractive index was lowered to 1,57. All three of these behaviors can be explained by air cavities within the sample. The cavities not only reduce the mass density and refractive index (which is one for air), but also lead to multiple reflections within the thin film itself. The X-rays get reflected on small film-air-interfaces were the film is porous due to a small change in refractive index and therefore lead to a less homogenous and more smeared out reflectivity pattern.

6.2.4 Fourier-transform infrared analysis

FTIR analysis has been conducted on samples prepared at 200 °C as well. The obtained transmission spectra can be seen in figure 6.7. The background spectrum is already subtracted and the data is baseline corrected.

Between 3550 and 3200 cm^{-1} typically N-H or O-H stretching occurs, at 3000 cm^{-1} the stretching between a C-H bond can be seen. The dip at 1660 cm^{-1} belongs to the stretching of the carbon double bond and is partly overlaps by the N-H bending which stretches from 1560 to 1640 cm^{-1}. The rather broad drop-off between 1000 and 650 cm^{-1} can be assigned to C-H out of plane bending. The small dip between 3000 and about 2900 cm^{-1} can be allocated to the C-H stretching.

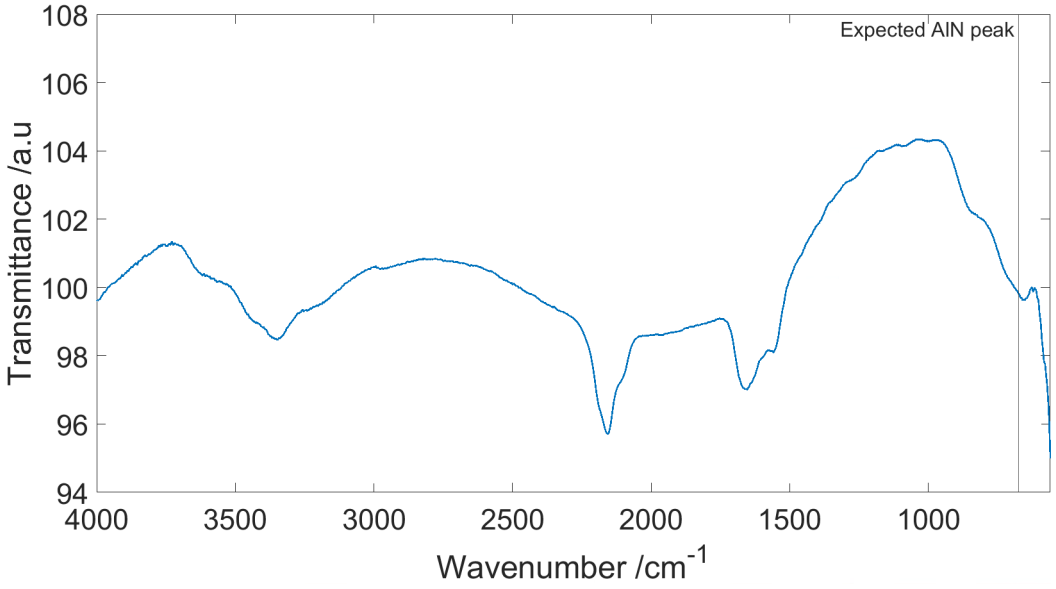

Figure 6.7: FTIR transmission spectra of deposited AlN at 200 °C and 560 cycles.

7 Conclusion and Outlook

Atomic layer deposition with aluminum precursor and nitrogen plasma was successfully performed at room temperature and at 200 °C. Depositions at room temperature showed a very high growth of about 0,6 nm/cycle. This growth per cycle is above the unit cell size of aluminum nitride, which means that a lot of residues are deposited on the surface. Therefore, no ideal recipe was determined.

An increase of the process temperature to 200 °C showed a decrease of growth to about 0,13 nm/cycle at 80 cycles. The ideal recipe was found to be 4/8/0,05/15 s (plasma dose/ purge /TMA dose/ purge), all four steps are in saturation and self-limiting growth can be achieved. The growth increased up to 0,15 nm/cycle for deposition done with 560 cycles.

Within the frame of this thesis, the atomic layer deposition system was remodeled. Existing lines were rearrangend, new lines and connections for additional precursor bottles were installed and the overall usability improved.

Thin film crystallinity was initially measured in the (002) and (222) direction with initial X-ray diffraction measurements. However, these results could not be replicated after the lockdown due to the covid-19 pandemic. Annealing measurements were performed, although no crystalline formation could be determined.

X-ray reflectivity measurements showed a homogeneous monolayer for thin films with a thickness of 10 nm. Thicker samples prepared exhibited multiple reflections and high surface roughness. The films underwent aging effects and showed an increase in film thickness and a change in color. The mass density was determined to be 3,58 g/cm^3.

Fourier transform infrared spectroscopy showed several bonds between nitrogen, hydrogen and oxygen atoms, indicating the existance of organic residues in the sample.

Depositions with titanium precursor could not be conducted successfully.

The next step would be to investige further into the problem of failed titanium deposition and then determine the saturation curves in order to obtain an optimized recipe. Aluminum titanium nitride films with different compososition ratios could then be produced and analyzed in terms of electrical, optical und thermal properties in order to obtain desired thin film characteristics.

Bibliography

[1] Nicola Pinna and Mato Knez. *Atomic Layer Deposition of Nanostructured Materials*. Jan. 2012. DOI: 10.1002/9783527639915.

[2] H.C.M. Knoops et al. *Handbook of Crystal Growth: Thin Films and Epitaxy: Second Edition*. Vol. 3. Jan. 2014, pp. 1101–1134.

[3] Harald Profijt et al. "Plasma-Assisted Atomic Layer Deposition: Basics, Opportunities, and Challenges." In: *Journal of Vacuum Science and Technology A: Vacuum, Surfaces, and Films* 29 (Sept. 2011), pp. 050801–050801. DOI: 10.1116/1.3609974.

[4] R. D. Clark et al. "(Invited) Process and Integration of Dielectrics Required for 10nm and Beyond Scaling." In: *ECS Transactions* 72.2 (2016), pp. 319–327. DOI: 10.1149/07202.0319ecst. URL: https://doi.org/10.1149%2F07202.0319ecst.

[5] Hausmann Dennis. *How Atomic Layer Deposition Works*. May 2018. URL: https://semiengineering.com/a-look-at-atomic-layer-deposition-2/ (visited on 04/02/2020).

[6] C.A.A Dingemans G. van Helvoirt. "Plasma-Assisted ALD for the Conformal Deposition of SiO2: Process, Material and Electronic Properties." In: *Journal of The Electrochemical Society* 159.3 (2012), H277–H285. DOI: 10.1149/2.067203jes. URL: https://doi.org/10.1149%5C%2F2.067203jes.

[7] Eindhoven TU. *Nanofacturing*. May 2018. URL: http://www.nano%20manufacturing.nl/ALE/ (visited on 04/02/2020).

[8] Ju Youn Kim et al. "Remote plasma enhanced atomic layer deposition of TiN thin films using metalorganic precursor." In: *Journal of Vacuum Science & Technology A* 22.1 (2004), pp. 8–12. DOI: 10.1116/1.1624285. URL: https://doi.org/10.1116/1.1624285.

[9] J. Musschoot et al. "Atomic layer deposition of titanium nitride from TDMAT precursor." In: *Microelectronic Engineering* 86.1 (2009), pp. 72–77. ISSN: 0167-9317. DOI: https://doi.org/10.1016/j.mee.2008.09.036. URL: http://www.sciencedirect.com/science/article/pii/S0167931708004292.

[10] Harm Knoops et al. "Status and prospects of plasma-assisted atomic layer deposition." In: *Journal of Vacuum Science and Technology A Vacuum Surfaces and Films* 37 (Mar. 2019), p. 030902. DOI: 10.1116/1.5088582.

[11] D Nilsson, E Janzén, and A Kakanakova-Georgieva. "Lattice parameters of AlN bulk, homoepitaxial and heteroepitaxial material." In: *Journal of Physics D: Applied Physics* 49.17 (Apr. 2016), p. 175108. DOI: 10.1088/0022-3727/49/17/175108. URL: https://doi.org/10.1088%5C%2F0022-3727%5C%2F49%5C%2F17%5C%2F175108.

[12] Hong Chen et al. "Band gap engineering in amorphous AlxGa1-xN: Experiment and ab initio calculations." In: *Applied Physics Letters* 77.8 (2000), pp. 1117–1119. DOI: 10.1063/1.1289496. URL: https://doi.org/10.1063/1.1289496.

[13] Dong Liu et al. "226 nm AlGaN/AlN UV LEDs using p-type Si for hole injection and UV reflection." In: *Applied Physics Letters* 113.1 (2018), p. 011111. DOI: 10.1063/1.5038044. URL: https://doi.org/10.1063/1.5038044.

[14] A. Ababneh et al. "Optical characterization of sputtered aluminum nitride thin films – correlating refractive index with degree of c-axis orientation." In: *Thin Solid Films* 693 (2020), p. 137701. DOI: https://doi.org/10.1016/j.tsf.2019.137701. URL: http://www.sciencedirect.com/science/article/pii/S004060901930728X.

[15] Mustafa Alevli et al. "Structural properties of AlN films deposited by plasma-enhanced atomic layer deposition at different growth temperatures." In: *Physica Status Solidi Applied Research* 209 (Feb. 2012), pp. 266–271. DOI: 10.1002/pssa.201127430.

[16] Alexander Pyymaki Perros et al. "Influence of plasma chemistry on impurity incorporation in AlN prepared by plasma enhanced atomic layer deposition." In: *Journal of Physics D: Applied Physics* 46.50 (Nov. 2013), p. 505502. DOI: 10.1088/0022-3727/46/50/505502. URL: https://doi.org/10.1088%2F0022-3727%2F46%2F50%2F505502.

[17] Markus Bosund et al. "Properties of AlN grown by plasma enhanced atomic layer deposition." In: *Applied Surface Science* 257.17 (2011), pp. 7827–7830. ISSN: 0169-4332. DOI: https://doi.org/10.1016/j.apsusc.2011.04.037. URL: http://www.sciencedirect.com/science/article/pii/S016943321100571X.

[18] V. I. Shapovalov et al. "Crystal structure and mechanical properties of titanium nitride films synthesized by magnetron sputtering with a hot target." In: *Glass Physics and Chemistry* 43 (2017), pp. 477–479. DOI: 10.1134/S1087659617050157.

[19] Wen-Jun Chou, Ge-Ping Yu, and Jia-Hong Huang. "Mechanical properties of TiN thin film coatings on 304 stainless steel substrates." In: *Surface and Coatings Technology* 149.1 (2002), pp. 7–13. ISSN: 0257-8972. DOI: https://doi.org/10.1016/S0257-8972(01)01382-2. URL: http://www.sciencedirect.com/science/article/pii/S0257897201013822.

[20] Gerritsen Eric et al. "Evolution of materials technology for stacked-capacitors in 65nm embedded-DRAM." In: *Solid-State Electronics* 49.11 (2005). Special Issue:Papers selected from the 1st International Conference on Memory Technology and Design - ICMTD'05, pp. 1767–1775. ISSN: 0038-1101. DOI: https://doi.org/10.1016/j.sse.2005.10.024. URL: http://www.sciencedirect.com/science/article/pii/S0038110105002674.

[21] W. Spengler et al. "Raman scattering, superconductivity, and phonon density of states of stoichiometric and nonstoichiometric TiN." In: *Phys. Rev. B* 17 (3 Feb. 1978), pp. 1095–1101. DOI: 10.1103/PhysRevB.17.1095. URL: https://link.aps.org/doi/10.1103/PhysRevB.17.1095.

[22] J.B. Ketterson. *The Physics of Solids*. OUP Oxford, 2016. ISBN: 9780191060564.

[23] P. Patsalas and S. Logothetidis. "Optical, electronic, and transport properties of nanocrystalline titanium nitride thin films." In: *Journal of Applied Physics* 90.9 (2001), pp. 4725–4734. DOI: 10.1063/1.1403677. URL: https://doi.org/10.1063/1.1403677.

[24] J. Musschoot et al. "Atomic layer deposition of titanium nitride from TDMAT precursor." In: *Microelectronic Engineering* 86.1 (2009), pp. 72–77. ISSN: 0167-9317. DOI: https://doi.org/10.1016/j.mee.2008.09.036. URL: http://www.sciencedirect.com/science/article/pii/S0167931708004292.

[25] Igor Krylov et al. "Obtaining low resistivity (100 mikro-Ohm-cm) TiN films by plasma enhanced atomic layer deposition using a metalorganic precursor." In: *Journal of Vacuum Science & Technology A* 36.5 (2018), p. 051505. DOI: 10.1116/1.5035422.

[26] Ju Youn Kim et al. "Remote plasma enhanced atomic layer deposition of TiN thin films using metalorganic precursor." In: *Journal of Vacuum Science & Technology A* 22.1 (2004), pp. 8–12. DOI: 10.1116/1.1624285.

[27] Yong Ju Lee and Sang-Won Kang. "Ti-Al-N Thin Films Prepared by the Combination of Metallorganic Plasma-Enhanced Atomic Layer Deposition of Al and TiN." In: *Electrochemical and Solid-State Letters* 6.5 (2003), p. C70. DOI: 10.1149/1.1561282. URL: https://doi.org/10.1149%5C%2F1.1561282.

[28] Toshiaki Fujita, Hiroshi Tanaka, and Noriaki Nagaotomo. *METAL-NITRIDE THERMISTOR MATERIAL, MANUFACTURING METHOD THEREFOR, AND FILM-TYPE THERMISTOR SENSOR*. 2013.

[29] Eun-Young Yun et al. "Electrical and Corrosion Properties of Titanium Aluminum Nitride Thin Films Prepared by Plasma-Enhanced Atomic Layer Deposition." In: *Journal of Materials Science & Technology* 33.3 (2017), pp. 295–299. ISSN: 1005-0302. DOI: https://doi.org/10.1016/j.jmst.2016.11.027. URL: http://www.sciencedirect.com/science/article/pii/S1005030216302419.

[30] P.R. Griffiths. *Fourier transform infrared spectrometry*. eng. Second edition. Chemical analysis 171. 2007. ISBN: 9780470106310.

[31] J. J. Ojeda and Maria Dittrich. *Fourier Transform Infrared Spectroscopy for Molecular Analysis of Microbial Cells*. Ed. by Ali Navid. Totowa, NJ: Humana Press, 2012, pp. 187–211. ISBN: 978-1-61779-827-6. DOI: 10.1007/978-1-61779-827-6_8. URL: https://doi.org/10.1007/978-1-61779-827-6_8.

[32] J. A. Woollam. *Ellipsometry tutorial*. URL: https://www.jawoollam.com/resources/ellipsometry-tutorial (visited on 06/04/2020).

[33] C. Suryanarayana and Grant Norton M. *X-Ray Diffraction - A Practical Approach*. eng. First edition. 1998. ISBN: 978-0-306-45744-9.

[34] Jean Daillant and Alain Gibaud. *X-Ray and Neutron Reflectivity: Principles and Applications*. Vol. 58. Jan. 2008. DOI: 10.1007/3-540-48696-8.

[35] Richard Berger. "Nano-Porous Zinc Oxide via Molecular Layer Deposition." MA thesis. TU Graz, Mar. 2019.

[36] M. Yasaka. "X-ray thin-film measurement techniques 5: X-ray reflectivity measurement." In: *The Rigaku Journal* 26(2) (2010).

[37] R. Resel. *X-ray and meutron scattering, lecture*. 2019.

[38] *Ultrahochreine Membranventile*. Swagelok, 2019. URL: https://www.swagelok.com/downloads/WebCatalogs/en/MS-02-301.PDF (visited on 07/10/2020).

[39] *Tetrakis-Dimethylamino Titanium(TDMAT) extrema grade*. Versum Materials, 2017. URL: https://v8cnuz00-a.akamaihd.net/wp-content/uploads/2017/01/tetrakisdimethylamino-titanium-tdmat%5C--extrema-w.pdf (visited on 07/10/2020).

[40] *Trimethylaluminum, electronic grade*. Sigma Aldrich, 2020. URL: https://www.sigmaaldrich.com/catalog/product/aldrich/j100013?lang=de&region=AT (visited on 07/10/2020).

[41] Ali Haider, Seda Kizir, and Necmi Biyikli. "Low-temperature self-limiting atomic layer deposition of wurtzite InN on Si(100)." In: *AIP Advances* 6.4 (2016), p. 045203. DOI: 10.1063/1.4946786. URL: https://doi.org/10.1063/1.4946786.

[42] Hao Van Bui et al. "Initial growth, refractive index, and crystallinity of thermal and plasma-enhanced atomic layer deposition AlN films." In: *Journal of Vacuum Science & Technology A* 33.1 (2015), 01A111. DOI: 10.1116/1.4898434.

[43] Jebreel M. Khoshman and Martin E. Kordesch. "Optical characterization of sputtered amorphous aluminum nitride thin films by spectroscopic ellipsometry." In: *Journal of Non-Crystalline Solids* 351.40 (2005), pp. 3334–3340. ISSN: 0022-3093. DOI: https://doi.org/10.1016/j.jnoncrysol.2005.08.009. URL: http://www.sciencedirect.com/science/article/pii/S0022309305006101.

[44] Duo Cao et al. "Effects of rapid thermal annealing on the properties of AlN films deposited by PEALD on AlGaN/GaN heterostructures." In: *RSC Adv.* 5 (47 2015), pp. 37881–37886. DOI: 10.1039/C5RA04728E. URL: http://dx.doi.org/10.1039/C5RA04728E.

[45] Institut für Arbeitsschutz der Deutschen Gesetzlichen Unfallversicherung. *Aluminiumnitrid GESTIS-Stoffdatenbank*. URL: http://gestis.itrust.de/nxt/gateway.dll/gestis_de/004980.xml?f=templates%5C$fn=default.htm%5C$3.0 (visited on 07/30/2020).